

# Prediction and Validation of Aerodynamic Characteristics for a Generic UCAV Configuration with Trailing-Edge Flaps

Michael E. Young,<sup>\*</sup>

*Defence Science and Technology Organisation, Melbourne, Victoria, 3207, Australia*

Mehdi Ghoreyshi,<sup>†</sup> Adam Jirásek,<sup>‡</sup> and Russell M. Cummings<sup>§</sup>

*U.S. Air Force Academy, Colorado, 80840-6400, USA*

This study focuses on the computational fluid dynamics prediction and validation against wind tunnel data, of the aerodynamic static and dynamic forces on the Stability and Control CONfiguration (SACCON) uninhabited combat air vehicle (UCAV) geometry with the addition of two trailing edge control surfaces on each wing. The vehicle exhibits significant nonlinear aerodynamic characteristics with respect to angle of attack, control surface deflections and frequency of motion even at low angles of attack, which makes the task of predicting the aerodynamic characteristics very complicated. A hybrid unstructured overset mesh was generated to simulate, in the Cobalt flow solver, the flow fields around the vehicle and to allow movement of the control surfaces. The results include comparisons between computational aerodynamic predictions and static and dynamic experimental data at low speeds. Predictions are shown for different turbulence models at selected flight conditions. Compared quantities include the force and moment coefficients and surface pressure tap data taken at four stations on the fuselage and wing. Static experiments correspond to different control surface settings at low to high angles of attack and sideslip. Dynamic tests were performed in pitch and yaw directions and at different oscillation frequencies. Finally, the effect of the overset method compared with conventional single grids was also investigated.

## Nomenclature

$C_A$	Axial force coefficient ( $= -C_X$ )
$C_D$	Drag coefficient ( $= -C_{X_w}$ )
$C_L$	Lift coefficient ( $= -C_{Z_w}$ )
$C_l$	Body axes rolling moment coefficient
$C_{l_w}$	Wind axes rolling moment coefficient
$C_m$	Body axes pitching moment coefficient
$C_{m_w}$	Wind axes pitching moment coefficient
$C_N$	Normal force coefficient ( $= -C_Z$ )
$C_n$	Body axes yawing moment coefficient
$C_{n_w}$	Wind axes yawing moment coefficient

<sup>\*</sup>Senior Aerospace Engineer, Aerospace Division, AIAA Member.

<sup>†</sup>Senior Aerospace Engineer, High Performance Computing Research Center, Senior AIAA Member

<sup>‡</sup>Research Fellow, High Performance Computing Research Center, Senior AIAA Member

<sup>§</sup>Professor of Aeronautics, High Performance Computing Research Center, AIAA Associate Fellow

Distribution A. Approved for Public Release. Distribution unlimited.



$C_p$	Pressure coefficient
$C_X$	Body axes $X$ -force coefficient ( $= -C_A$ )
$C_{X_w}$	Wind axes $X$ -force coefficient ( $= -C_D$ )
$C_Y$	Body axes $Y$ -force coefficient
$C_{Y_w}$	Wind axes $Y$ -force coefficient
$C_Z$	Body axes $Z$ -force coefficient
$C_{Z_w}$	Wind axes $Z$ -force coefficient ( $= -C_L$ )
$t$	Time
$y+$	Non-dimensional wall normal distance

#### *Greek*

$\alpha$	Angle of attack
$\beta$	Angle of sideslip
$\theta$	Pitch angle
$\phi$	Roll angle
$\psi$	Yaw angle

## I. Introduction

The NATO AVT-201 task group, “Extended Assessment of Stability and Control Prediction Methods for NATO Air Vehicles”, was instigated with the objective of determining an overall strategy for creating stability and control databases for vehicle simulation, including the deflection of control surfaces.<sup>1</sup> The AVT-201 task follows on from AVT-161, which provided an assessment of the state of the art for using CFD to predict the stability and control characteristics of air vehicles. The extensive set of results from the AVT-161 task group can be found in papers published at the 28th AIAA Applied Aerodynamics Conference in 2010, in the proceedings of the NATO RTO-AVT Specialists Meeting held in October 2011 (RTO MP-AVT-189), in a special issue of AIAA’s Journal of Aircraft published in November–December of 2012 (v.49, n.6), and in various other fora.

Both AVT-201 and AVT-161 investigated a generic uninhabited combat aerial vehicle (UCAV) configuration known as SACCON (Stability and Control CONFIGuration), and performed both static and dynamic cases; however, AVT-201 has been extended to include the effect of control surfaces. As part of this endeavour, extensive wind tunnel testing of the SACCON was conducted by the German Aerospace Centre (Deutsches Zentrum für Luft- und Raumfahrt, DLR) at the German-Dutch wind tunnel facility at Braunschweig (DNW-NWB).

The SACCON was developed as an unclassified, UCAV-representative design, that would challenge the state-of-the-art in CFD.<sup>2,3</sup> The 53 degree angle of sweep leads to complex vortex dominated flow even at moderate angles of attack as can be seen in figure 1. The overall configuration and reference geometry can be seen in figure 2.

Previous CFD and experimental work on the SACCON looked at the aerodynamic loading with control surfaces undeflected.<sup>4,5,6,7,8,9</sup> The F19 configuration of the SACCON model as tested at Braunschweig includes inboard and outboard control surfaces on the trailing edge of each wing, giving a total of four control surfaces. The control surfaces have a nominal hingeline of 75% chord. Details of the control surface geometry of the wind tunnel model can be seen in figure 3a. In order to model the control surfaces, it was decided to use the overset method available in Cobalt. This gives flexibility in grid generation, and also allows the grid to be used for the development of reduced order models that need to model the dynamic motion of the control surface relative to the wing, something that cannot be done when using a single (i.e. non-overset) static grid.

This paper documents the validation of the Cobalt computational fluid dynamics (CFD) code against a subset of the wind tunnel data. It primarily looks at the effects of angle of attack for the control surfaces both undeflected and deflected, and the effects of sideslip and dynamic pitch and yaw motions for the control surfaces undeflected. It then assesses the effect of using the overset method versus a conventional single grid for the static cases with control surfaces both deflected and undeflected.



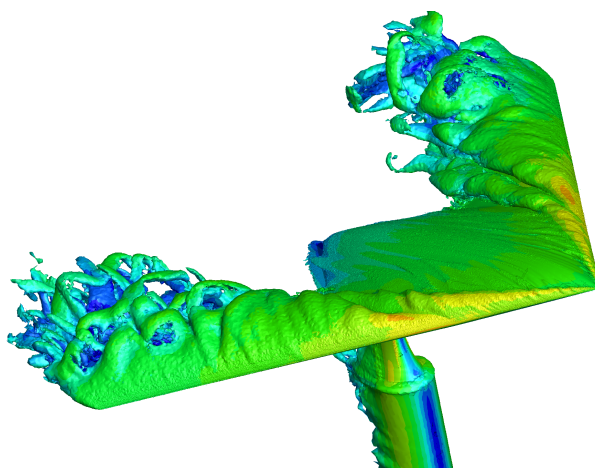


Figure 1. Illustrating the vortex dominated flow at an angle of attack of 16 degrees. DDES-SARC turbulence model used. Isosurface of vorticity magnitude shown coloured by velocity magnitude.

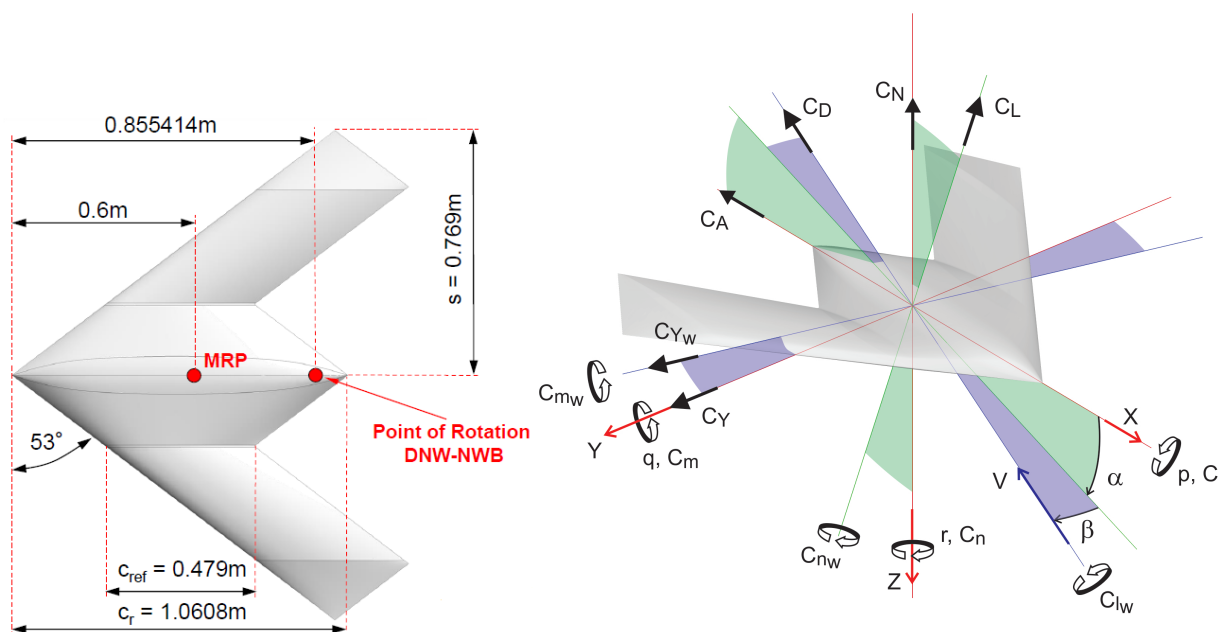


Image from Cummings and Schütte (2012)<sup>10</sup>

Image courtesy of D. Vicroy, NASA

Figure 2. Geometry, reference data, and axis system for the SACCON F19 wind tunnel model.

## II. Experimental Tests and Data

The experimental tests were conducted in the German-Dutch Wind Tunnels' Braunschweig (DNW-NWB) facility.<sup>3,11</sup> The flow velocity was approximately  $50 \text{ m s}^{-1}$ , giving a Reynolds number of approximately  $1.6 \times 10^6$  based on the reference chord length of 0.479m. Based on experience from the AVT-161 test programme, the boundary layer was tripped to fully turbulent using carborundum grit particles on the wing leading edge.

Static tests were conducted through angle of attack and angle of sideslip sweeps, both with various control surface combinations. Dynamic tests were performed with pitch and yaw oscillations. The subset of cases that are examined in this paper are listed in table 1. Data available from the experiments include six axis force and moment coefficients, and pressure coefficients at the pressure tap locations indicated in figure 3b.



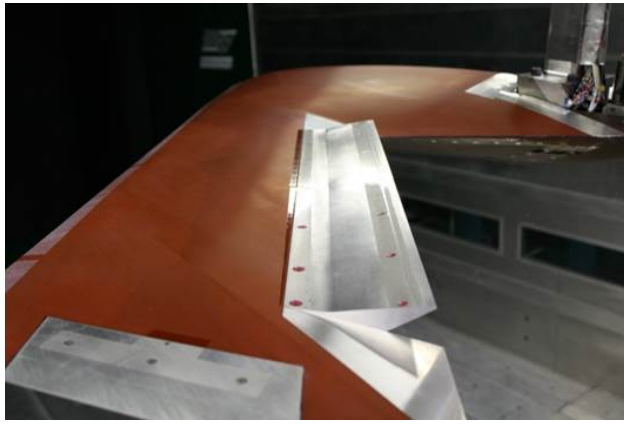


Image courtesy of DLR

(a) Detail of starboard control surfaces, shown with +20 degrees deflection

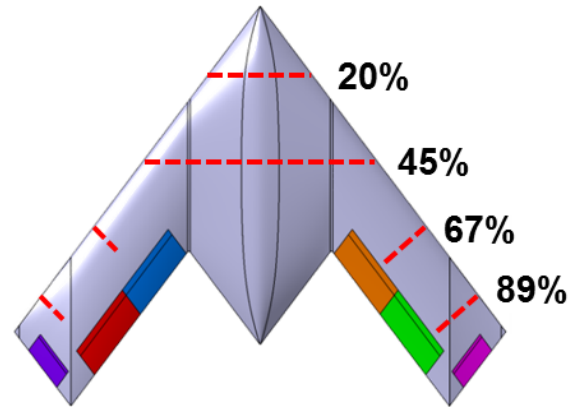


Image from Huber, Vicroy et al. (2014)<sup>3</sup>

(b) Location of pressure tap locations for the SACCON F19 low speed wind tunnel model

**Figure 3. The SACCON F19 wind tunnel model.**

The reference area is  $0.77 \text{ m}^2$ . The reference chord,  $c_{\text{ref}}$ , and halfspan,  $s$ , as indicated in figure 2a were used to non-dimensionalise the longitudinal and lateral/directional coefficients, respectively. The moment reference point (MRP) for all cases and the point of rotation for the dynamic tests are also indicated in figure 2a. The axis system is indicated in figure 2b. The CFD results presented herein are consistent with the wind tunnel data in these definitions.

**Table 1. Low speed wind tunnel static angle of attack sweep test cases with control surface deflections.**

Test Number	Description	LOB	LIB	RIB	ROB
RN1001	Angle of attack sweep	–	–	–	–
RN1103	Angle of attack sweep	–20	–20	+20	+20
RN1007	Angle of sideslip sweep at $\alpha = 10$ degrees	–	–	–	–
RN1008	Angle of sideslip sweep at $\alpha = 14$ degrees	–	–	–	–
RN2342–50	Dynamic pitch oscillation, $\theta = 10 \pm 4.7$ degrees at 1 Hz	–	–	–	–
RN2351–59	Dynamic pitch oscillation, $\theta = 10 \pm 4.7$ degrees at 2 Hz	–	–	–	–
RN2270–78	Dynamic yaw oscillation, $\alpha = 10$ degrees, $\psi = \pm 5.0$ degrees at 1 Hz	–	–	–	–

### III. Numerical Method

#### III.A. CFD Solver

The flow solver used for this study is Cobalt version 6.0.<sup>12,13</sup> Cobalt solves the unsteady, three-dimensional and compressible Navier-Stokes equations in an inertial reference frame. The Navier-Stokes equations are discretised on arbitrary grid topologies using a cell-centered finite volume method. Second-order accuracy in space is achieved using the exact Riemann solver of Gottlieb and Groth,<sup>14</sup> and least squares gradient calculations using QR factorization. To accelerate the solution of the discretised system, a point-implicit method using analytic first-order inviscid and viscous Jacobians is implemented. A Newtonian sub-iteration method is used to improve time accuracy of the point-implicit method. Tomaro et al<sup>15</sup> converted the code from explicit to implicit, enabling Courant-Friedrichs-Lewy numbers as high as  $10^6$ . Available turbulence models include the Spalart-Allmaras (SA) model,<sup>16</sup> the Spalart-Allmaras model with rotation/curvature correction (SARC),<sup>17</sup> Wilcox's  $k-\omega$  model,<sup>18</sup> and Mentor's SST model,<sup>19</sup> as well as the delayed detached eddy simulation (DDES) implementations of the SA, SARC, and SST models. For details of the implementation



of the turbulence models, refer to the Cobalt User Manual.<sup>12</sup>

The Cobalt solver includes the option of an overset grid method that allows the independent translation and rotation of each grid around a fixed or moving hinge line. In this method, overlapping grids are generated individually, without the need to force grid points to be aligned with neighboring components. In Cobalt, the overlapping grids are treated as a single mesh using a grid-assembly process. This includes a hole-cutting procedure in overlapping regions and interpolation between overlapping grids. The translation and rotation of overset grids around the hinge line are input to the code using a grid control file (GCF). The hinge line is defined by a reference point and a vector combination. The rotations are right-handed and consist of angles in the order of pitch, yaw, and roll angle. These angles are calculated from the deflection angle of a control surface and the relative angles between the hinge line and grid coordinate axes.

### III.B. CFD Geometry

Unlike the computational investigations conducted by other members of AVT-201,<sup>20, 21, 22, 23, 24, 25, 26</sup> this study used the overset grid capabilities available in Cobalt in order to model the control surface deflections. The advantages of this approach were twofold: firstly, it reduces the onerous task of grid generation since one single set of grids can be used for all control surface deflections rather than requiring a new mesh to be generated for each case; secondly, it retains the flexibility of allowing time-dependent changes to the control surface deflections, which is a necessary element to investigating methods such as indicial functions. Indicial functions will be used to create reduced-order models (ROMs) for the control surface deflections in another element of this project.<sup>27</sup>

Such use of overset grids was demonstrated in Ghoreyshi et al.<sup>28</sup> The disadvantage of the overset approach, at least as required by Cobalt, is that it is necessary to create a chordwise gap between wing and control surface that is not present in the wind tunnel tests. In the current CFD geometry this gap was set to 2 mm (0.4% reference chord). The effect of different gap sizes was not studied with respect to the SACCON geometry, but is the subject of an ongoing study.<sup>29</sup> A second disadvantage of the overset method is that it also results in a significant computational overhead when compared to a single grid with similar resolution.

A complication for the generation of the control surface grids is that the actual model as tested in the wind tunnel obtained the different control surface deflections through interchangeable rather than hinged control surfaces. This is similar to the provided CAD geometry which contained separate elements for the deflected and undeflected control surfaces, rather than a single, rotating, element. Furthermore, the deflected control surface is not simply a rotation of the undeflected control surface about a given hingeline, but some deformation as well. This can be seen in figure 4.

Therefore, having decided to use the overset technique, the geometry required modification in order to do so. Firstly, hingelines were defined based on the differences between the deflected and undeflected CAD geometries. The control surfaces were then modified so as to have a semi-circular leading edge, which fit into the modified semi-circular trailing edge of the wing, with the 2 mm gap in between. In order to avoid intersection of the wing with deflected control surfaces, the inboard and outboard edges of the control surfaces had to be trimmed. This resulted in gaps slightly larger than in the original CAD geometry. Details of control surface geometry as modified for deflection using overset grids can be seen in figure 5.

Note, in the wind tunnel model, there are no spanwise gaps between the two control surfaces on the same wing when they are at the same deflection, nor between the control surfaces and wing when they are undeflected.

It was found in earlier studies<sup>6, 7</sup> that the inclusion of the sting geometry significantly modifies the flowfield, with particular influence on the pitching moment coefficient. Therefore, the sting is included in the geometry for the CFD simulation.

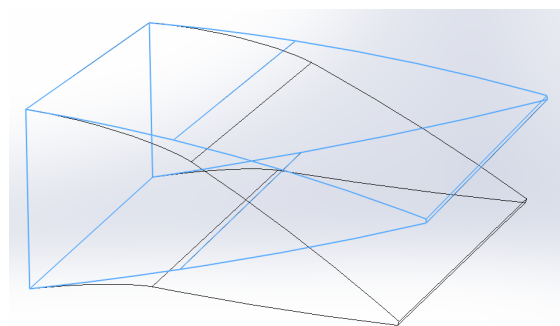


**Figure 4. Comparing the deflected (black) and undeflected (blue) control surfaces from the CAD geometry.**



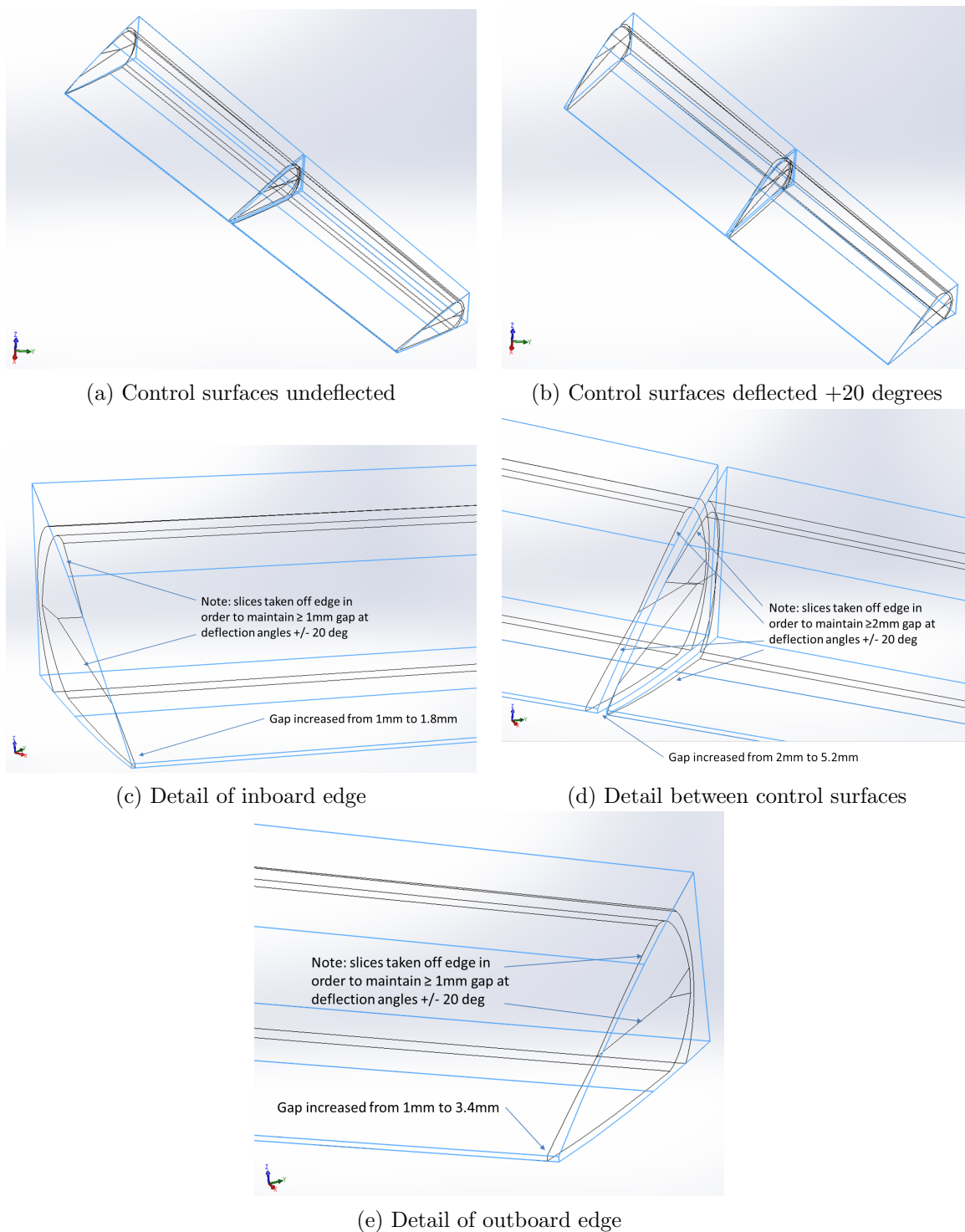


**Figure 5. Modifications to CAD geometry to facilitate control surface deflection using overset grids. Blue lines represent the original CAD geometry provided by DLR, black lines represent the modified geometry.**



### III.C. Grid

The geometry, as modified according to the previous section, was gridded with a Euler background mesh defined in ICEMCFD. Particular mesh refinement was concentrated around the leading edge of the wing, the trailing edge of the wing, in areas in which the overset grids occur (i.e. around the control surfaces), and a general refinement off the upper surface of the UCAV. This off body refinement allows the CFD to capture the vortices that develop on the SACCON configuration at higher angles of attack. The resulting grid can be seen in figure 6a. Detail of the surface grid near the control surfaces is shown in figure 6b. Chordwise cuts illustrating the overset grid stitching for the control surfaces can be seen in figure 6c and 6d, with the different colours denoting the separate contributing grids. The background mesh was then used by TRITET<sup>30,31</sup> to define the viscous boundary layer grid close to the surface. The resultant  $y+$  for the zero angle of attack case can be seen in figure 7.

The grid was created based on experience with previous grids generated for the SACCON configuration in previous studies,<sup>6</sup> and due to the very high resolution in this grid (the background mesh for the overset method contained 129 million cells, and each control surface grid contained 5.8 to 5.9 million cells), a mesh resolution study was not conducted. The grid has a farfield at 50 metres (104 chord lengths).

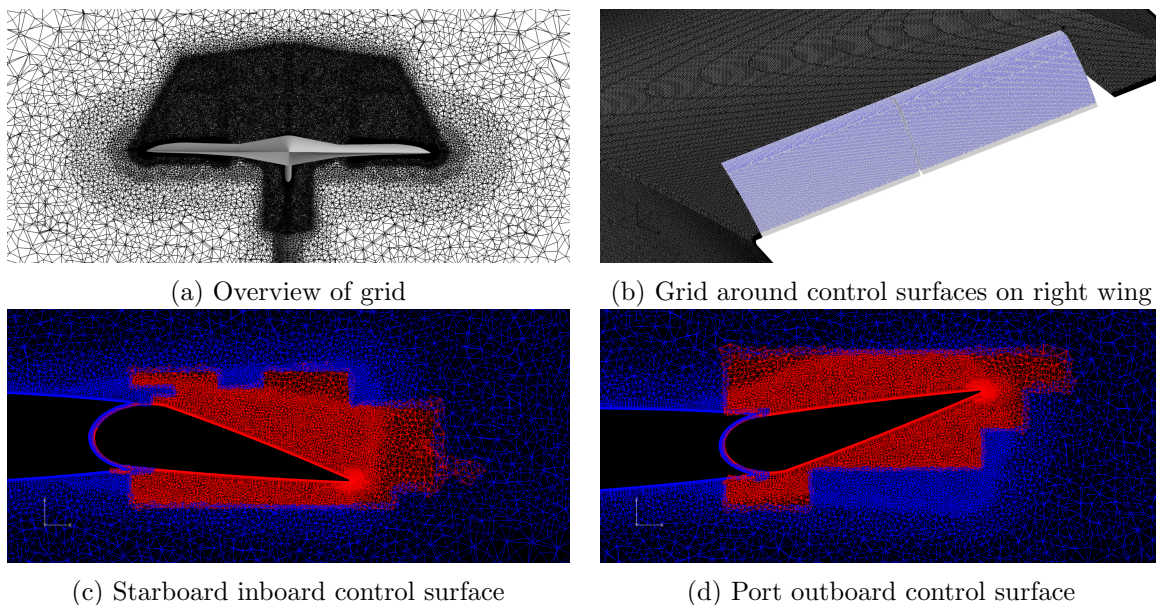


**Figure 6. Overset grid of the F19 model with control surfaces. Starboard control surfaces are deflected +20 degrees. Port control surfaces are deflected -20 degrees.**

### III.D. Solver Settings

There were effectively three categories of solution methods used with Cobalt in this study. A quasi-steady method in which the temporal accuracy was set to first order, the case was run with a CFL number of  $1 \times 10^6$ , and 1 Newton sub-iteration was used. This was the method used for most of the RANS cases. The unsteady method in which the temporal accuracy was set to second order, the timestep was defined, and 2 Newton sub-iterations were used. This was the method used for any DDES cases, and for some RANS cases to test the effect of unsteadiness on the solution. And the dynamic method, which was the same as the unsteady method, but with 5 Newton sub-iterations as recommended in the Cobalt User Manual.<sup>12</sup> This was the method used when there was rigid body motion, i.e. for the dynamic pitch and yaw cases. In all cases second order spatial accuracy was used.

The farfield boundary condition was set to a modified Riemann invariant, and the aircraft and its control surfaces were set to adiabatic no slip wall boundary conditions.

The undocumented “thin-gap” option was used for the overset grid. This option modifies the manner in which the hole cut algorithm works. The difference between using the default and thin-gap overset options can be seen in figure 8. Note, in particular, the difference in the gap between the control surface and the wing.



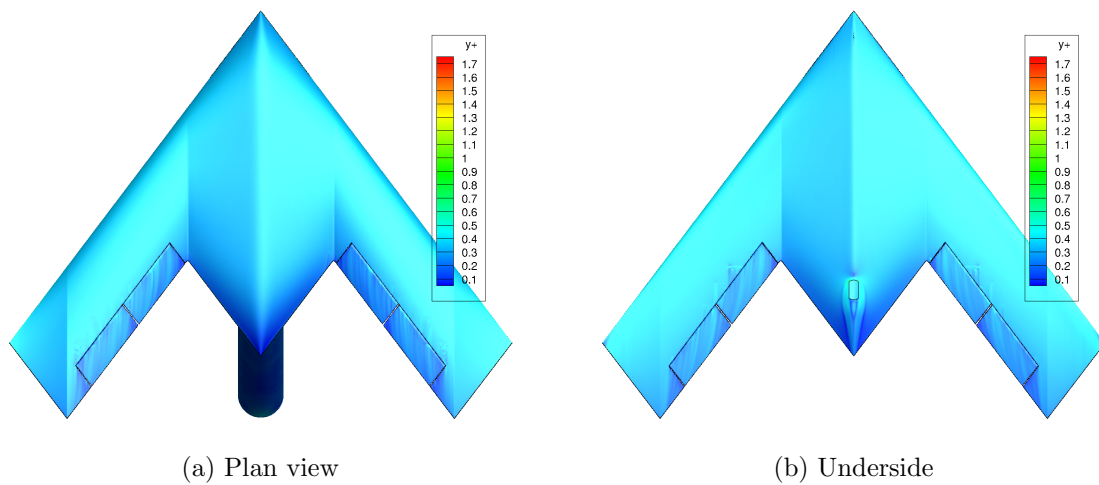


Figure 7.  $y^+$  of the grid. Control surfaces undeflected; angle of attack 0 degrees; SARC turbulence model.

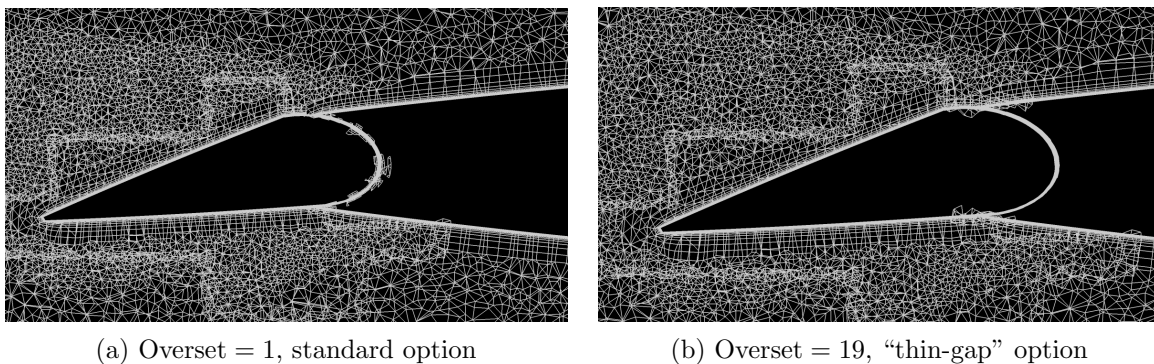


Figure 8. Illustrating the differences in the combined grid when using the different overset options.



### III.E. Turbulence Models

The SARC and SST RANS turbulence models and the DDES-SARC and DDES-SST hybrid models were tested. It was found that the SARC model performed well over a large portion of the angle of attack range, even in quasi-steady mode, and this model was the most extensively tested. The other models were tested at specific flow conditions to investigate whether they offered any improvement or variation compared with the SARC model. Due to computational resource constraints, alternative turbulence models could not be more fully tested.

## IV. Results and Discussion

This section presents the Cobalt results for the static and dynamic tests performed. Comparison of these results with other solvers used by partners in AVT-201 can be found in Jirasek et al.<sup>32</sup>

### IV.A. Static Results

#### IV.A.1. RN1001: Angle of Attack Sweep with Control Surfaces Undeflected

The overall force and moment coefficients for the RN1001 cases are shown in figure 9. The “error” bars depicted in figure 9 are not actually error bars, but rather indicate the standard deviation of the force or moment coefficients. For the experimental data, this was obtained over a measurement time of two seconds. Where there are bars on the computational data, this indicates that that condition was run in unsteady mode.

The initial sweep of cases used the SARC turbulence model at 5 degree increments from angle of attack of zero to 30 degrees, with finer resolution in angle of attack about the break in pitch moment from 14 to 18 degrees. Plots of surface pressure coefficient contours with streamlines are presented in the left column of figure 10. Plots comparing the surface pressure coefficient predicted by the CFD with the tapped locations from the experimental data are presented in the right column of figure 10.

As was seen in previously published results<sup>4,6,8</sup> the computational results underpredict the pitching moment coefficient,  $C_{m_w}$ , at angles of attack less than approximately 15 degrees. The SARC model is the worst performer of the models tested, but it still provides results similar to the best performing simulations from the references cited above. Both of the DDES models and the SST model perform better at the tested angle of attack of 10 degrees. The effects of turbulence model will be looked at more closely in the following subsection.

The SARC model does not capture the pitch break in the region of 16 to 17 degrees angle of attack particularly well. The drop in pitching moment from 16 to 16.5 degrees is small compared to the experimental data, and the flow appears to have moved to a different ‘mode’ by 17 degrees in the computational case, whereas it is not until approximately 19 degrees that the experimental data obtains the same pitching moment coefficient. This is correlated with the pressure coefficient plots in figures 10f to k. We can see in figure 10f that at 16 degrees angle of attack the pressure distribution matches the experimental data well. As we move to figure 10g depicting 16.25 degrees angle of attack, the outboard vortex appears to be losing strength in the experimental data (green dots) compared to the CFD results. The computationally derived flowfield changes markedly between 16.25 and 16.5 degrees angle of attack as can be seen in the plan view images in figures 10g and h. The inboard vortex weakens and the outboard vortex strengthens and moves forward. It appears, however, that the SARC results start to underestimate the strength of the vortices at 16.5 degrees, and by 17 degrees, the computational result is well underestimating the vortex strength at the 45% and 67% cuts. This continues at 18 degrees, and to a much lesser extent at 20 degrees. At 20 degrees and above, the movement and combining of vortices along the leading edge ceases and we have a single vortex originating at the nose. It would appear that, despite using a ‘steady’ temporal scheme, the SARC model manages to capture the dominant effect of that single vortex on the surface pressure, and resultant pitching moment coefficients.

The computational result matches the lift coefficient from experiment well until an angle of attack of 16.5 degrees, beyond which the computational result falls away before recovering somewhat from 20 to 30 degrees, whereas the experimental result continues to increase, albeit in decreasing amounts, until an angle of attack of approximately 26 degrees. This seems to have an effect on drag coefficient as well, where the drag coefficient from 18 to 25 degrees is less than experiment before matching again at 30 degrees. The use of the DDES-SARC model at 17 degrees only marginally improves the match in lift coefficient.



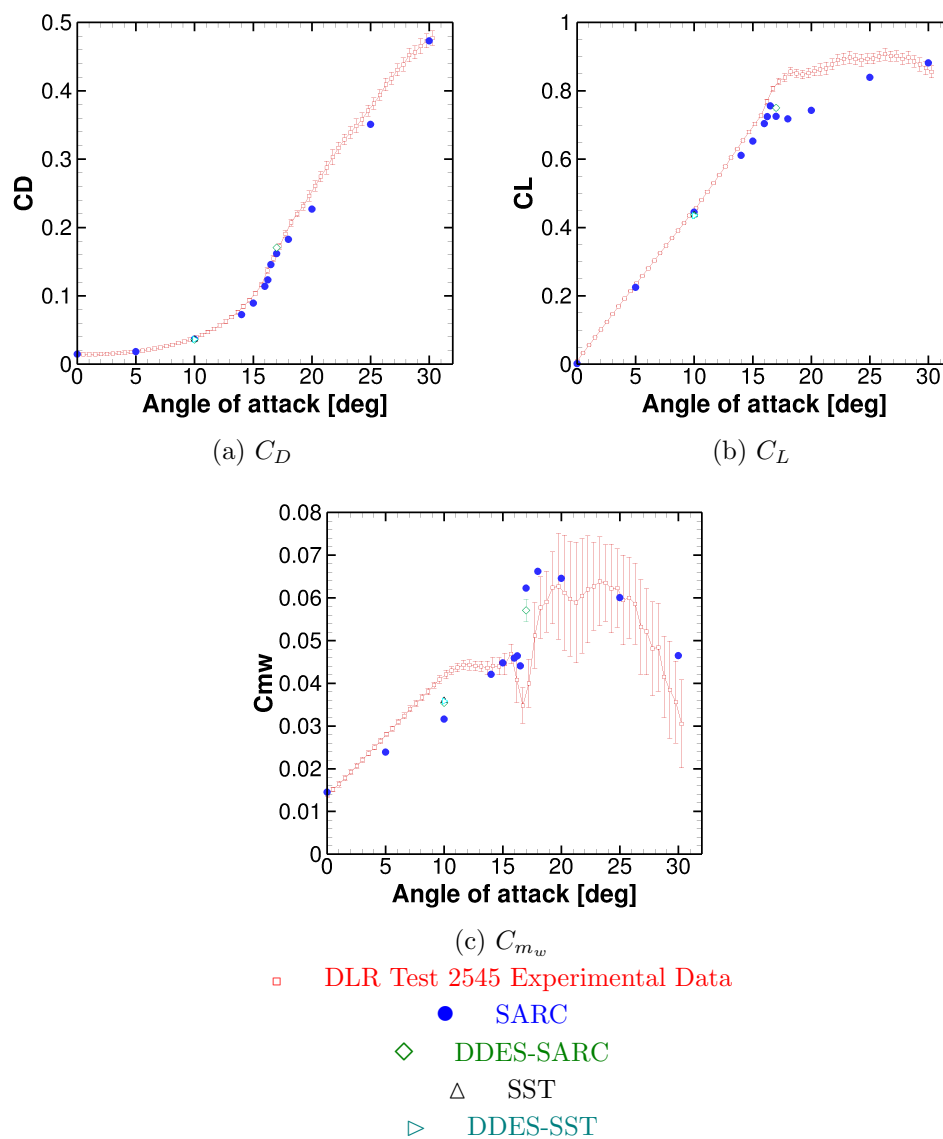


Figure 9. Force and moment coefficients for RN1001 (control surfaces undeflected, angle of attack sweep) cases.



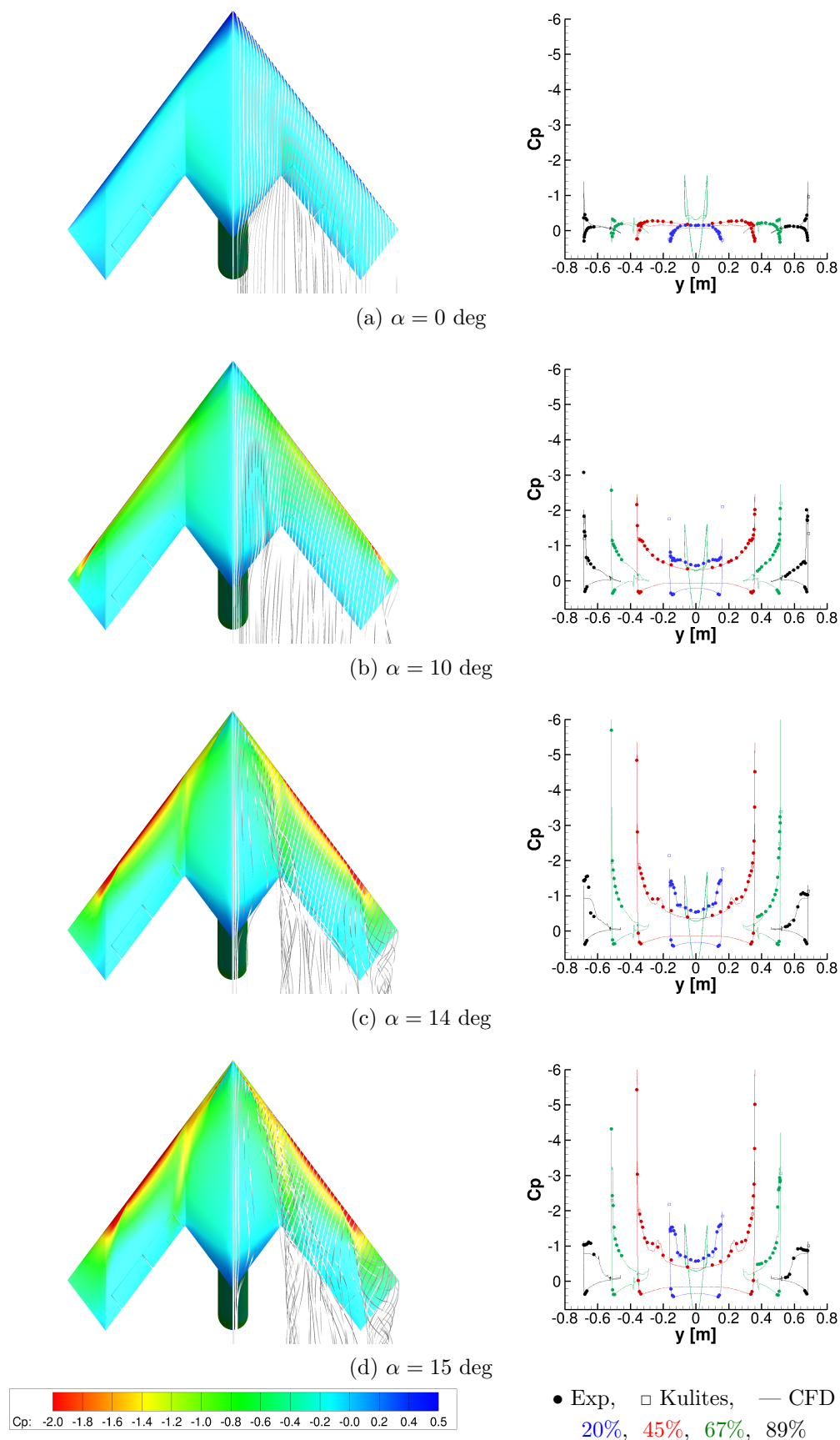
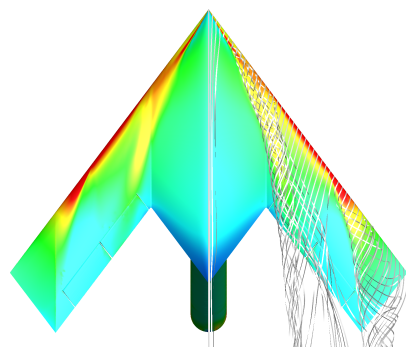
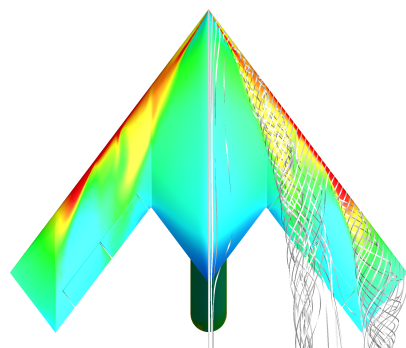
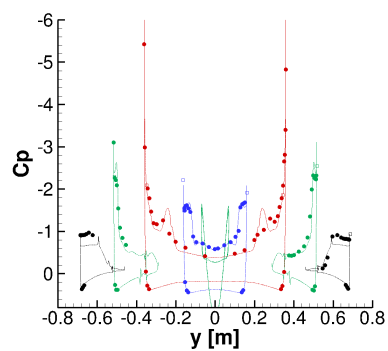


Figure 10. Pressure coefficients from the angle of attack sweep using the SARC turbulence model with no control surface deflections (RN1001).

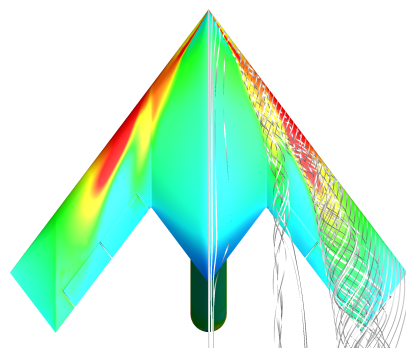
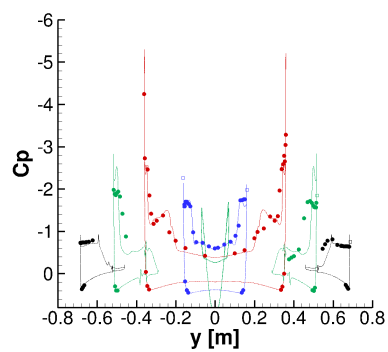




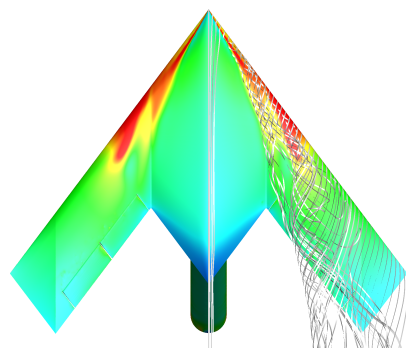
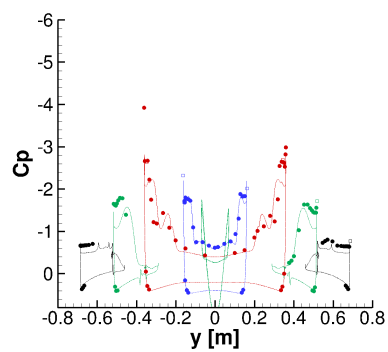
(e)  $\alpha = 16$  deg



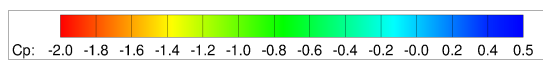
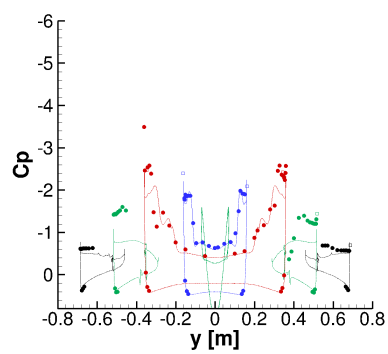
(f)  $\alpha = 16.25$  deg



(g)  $\alpha = 16.5$  deg

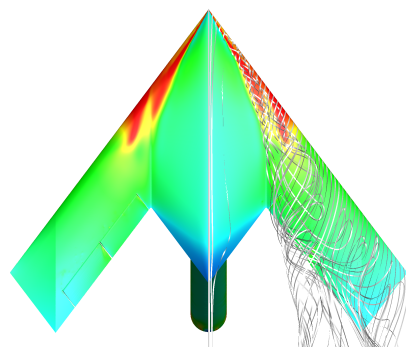


(h)  $\alpha = 17$  deg

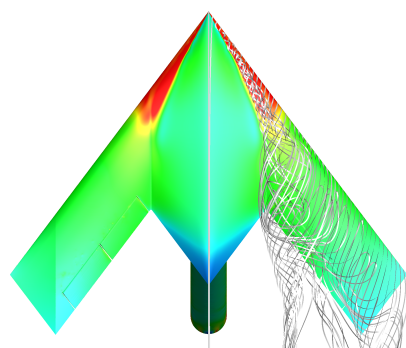
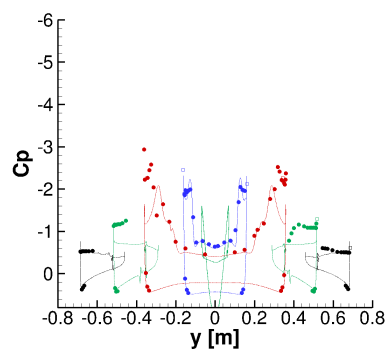


• Exp, □ Kulites, — CFD  
20%, 45%, 67%, 89%

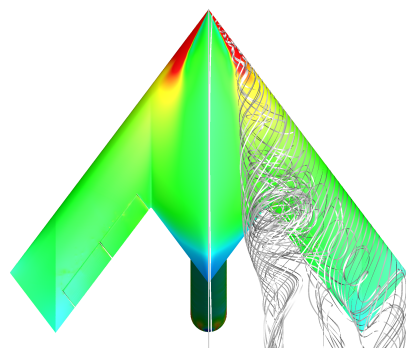
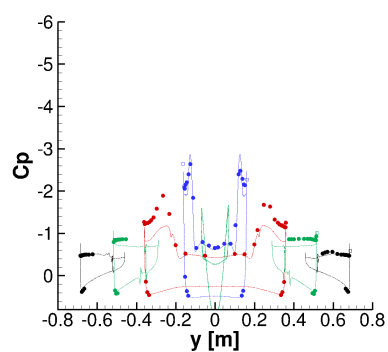




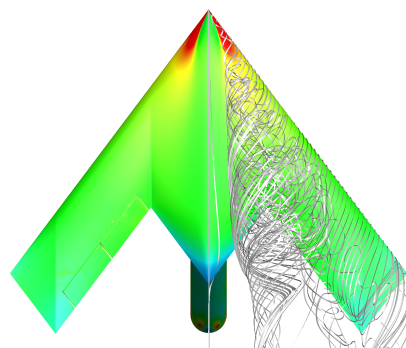
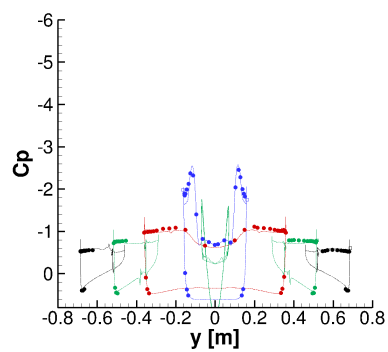
(i)  $\alpha = 18$  deg



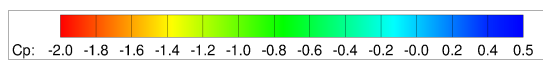
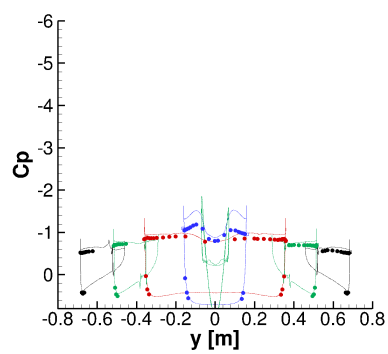
(j)  $\alpha = 20$  deg



(k)  $\alpha = 25$  deg



(l)  $\alpha = 30$  deg



• Exp, □ Kulites, — CFD  
20%, 45%, 67%, 89%



### Effect of Turbulence Model

Different turbulence models were used at certain flow conditions to ascertain their effect on the solution.

The poor match in pitching moment below 15 degrees prompted additional testing at 10 degrees angle of attack. It can be seen in figure 9 that all the alternative turbulence models tested (SST, DDES-SARC, and DDES-SST) give similarly improved pitching moment coefficient. Figure 11 compares the *difference* in surface pressure coefficient between the different models, e.g.  $C_{P_{SARC}} - C_{P_{DDES-SARC}}$ . The SARC model is compared to the SST model in figure 11a, the SARC model is compared to the DDES-SARC model in figure 11b, and the SST model is compared to the DDES-SST model in figure 11c. The most notable differences evident from figure 11 are, on the upper side, the location and intensity of the flowfield near the wingtip, and on the underside, in the flowfield downstream of the sting location. However, the variations exhibited by each model occur are inconsistent, and so it is not clear what the SARC model is ‘missing’.

The discrepancies in the pitch moment coefficient through the pitch break also prompted investigation of an angle of attack of 17 degrees using the DDES-SARC method. Figure 9 shows that the pitching moment coefficient for the DDES-SARC result is not significantly different to the SARC result when compared to the experimental data. However, the differences are more significant when comparing the surface pressure coefficient and flowfield for these cases, as seen in figure 12. The DDES-SARC result overpredicts the strength of the vortex at the 20% cut, but does a better job at the 45% cut. Both results seem to show that the vortices weaken too far forward, because the computational results at the 67% cut are too low. Inspecting the surface pressure contours on a qualitative level, the DDES-SARC case appears to show the vortices diffusing over the wing rather than abruptly stopping, possibly an indication of vortex breakdown that is not evident for the SARC model. Both models still contain discrepancies when compared to the surface tap data from the experiment. Note, the DDES-SARC data is not time-averaged, which means that it is not a direct comparison with the experimental data which is time-averaged over two seconds. The unsteadiness is evident in figure 9, in which the DDES-SARC point at  $\alpha = 17$  degrees has bars that represent the standard deviation of the coefficient, in this case over 3000 timesteps (1.5 seconds).

#### IV.A.2. RN1007: Angle of Sideslip Sweep at $\alpha = 10$ Degrees with Control Surfaces Undeflected

The overall force and moment coefficients for the RN1007 cases are shown in figure 13. The surface pressure coefficients and flowfield streamlines are shown in figure 14.

The effect of sideslip at this angle of attack is well predicted by the computational model. The changes in force and moment coefficients are very close to experiment. Aside from the absolute value of pitching moment coefficient being incorrect (as discussed earlier), the most significant discrepancy is the slope of the sideforce coefficient due to sideslip, where the computational result underpredicts the effect of sideslip. The pressure coefficients match very closely to the experimental data with the minor exception of not quite capturing the peak of the values of pressure coefficient of the port wing at 89%.

#### IV.A.3. RN1008: Angle of Sideslip Sweep at $\alpha = 14$ Degrees with Control Surfaces Undeflected

The overall force and moment coefficients for the RN1008 cases are shown in figure 15. The surface pressure coefficients and flowfield streamlines are shown in figure 16.

The experimental rolling and pitching moment coefficients in figure 15 reveal that the effect of sideslip is quite nonlinear at this angle of attack; however, the only computational case run was at 3 degrees angle of sideslip – within the linear range. At this single point, the effect of sideslip is well represented in the computational result, as per the case at 10 degrees angle of attack.

#### IV.A.4. RN1103: Angle of Attack Sweep with Control Surfaces Fully Deflected to Generate Maximum Roll Moment

The overall force and moment coefficients for the RN1103 cases are shown in figure 17. The surface pressure coefficients and flowfield streamlines are shown in figure 18.

The drag, sideforce and yawing moment coefficients are all close to the experimental data. Interestingly, the pitching moment coefficient is a lot closer to the experimental data than was found for the cases with undeflected control surfaces. This suggests that the flow induced by the deflection of the control surfaces is more dominant than the cause of the discrepancy in pitching moment. Although we do not have the same resolution in angle of attack through the pitch break as for the undeflected case, it again appears as if the



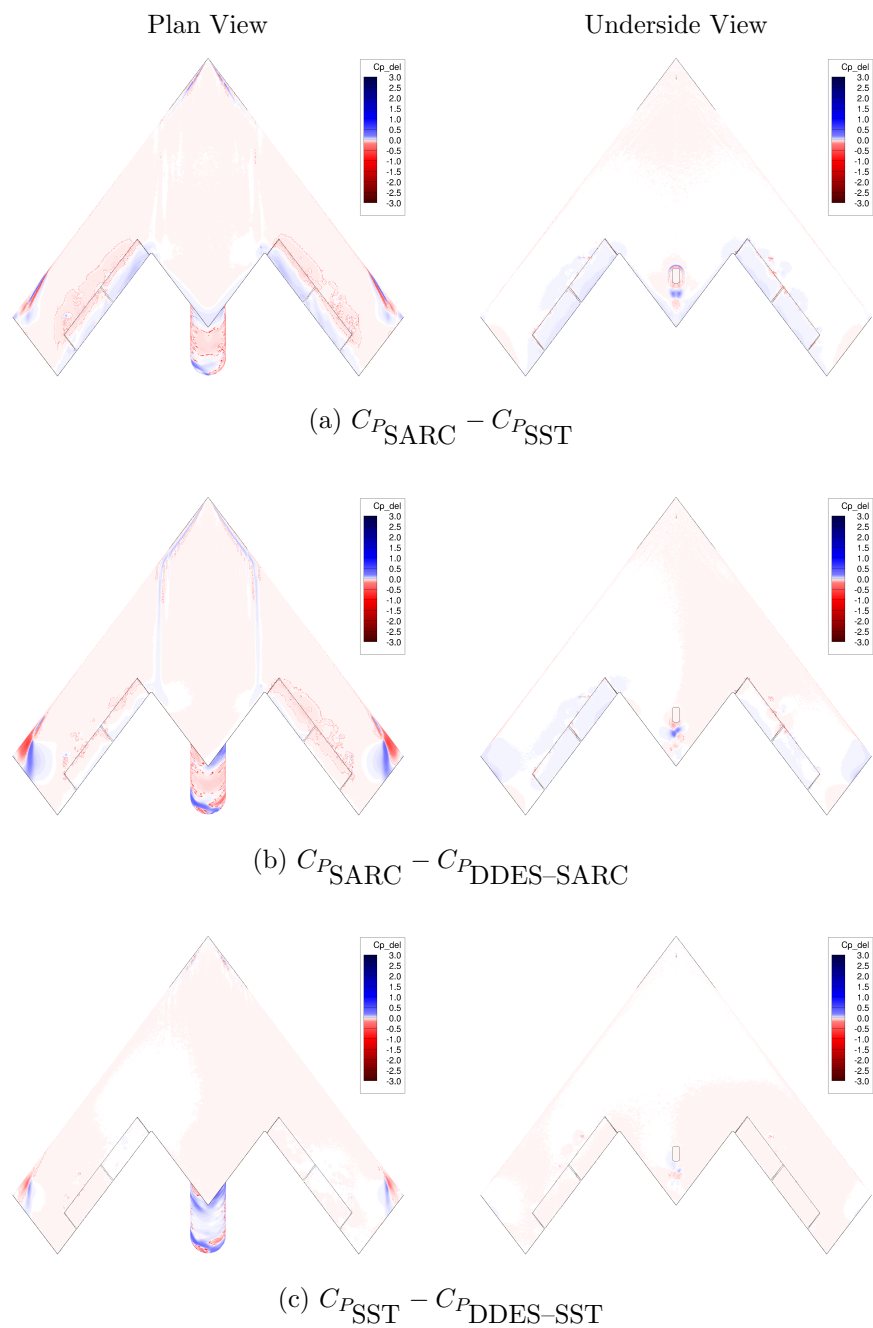


Figure 11. Comparing delta in pressure coefficients for different turbulence models for the RN1001 case at an angle of attack of 10 degrees.



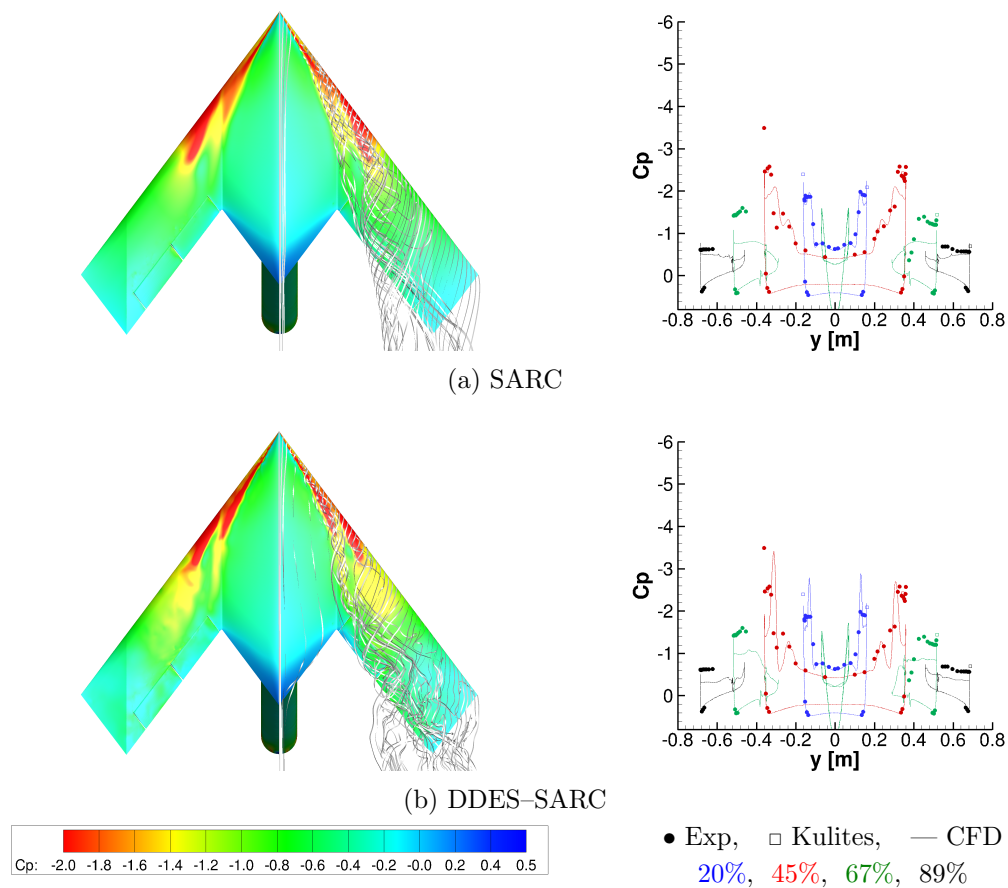


Figure 12. Comparing pressure coefficients for different turbulence models for the RN1001 case at an angle of attack of 17 degrees.



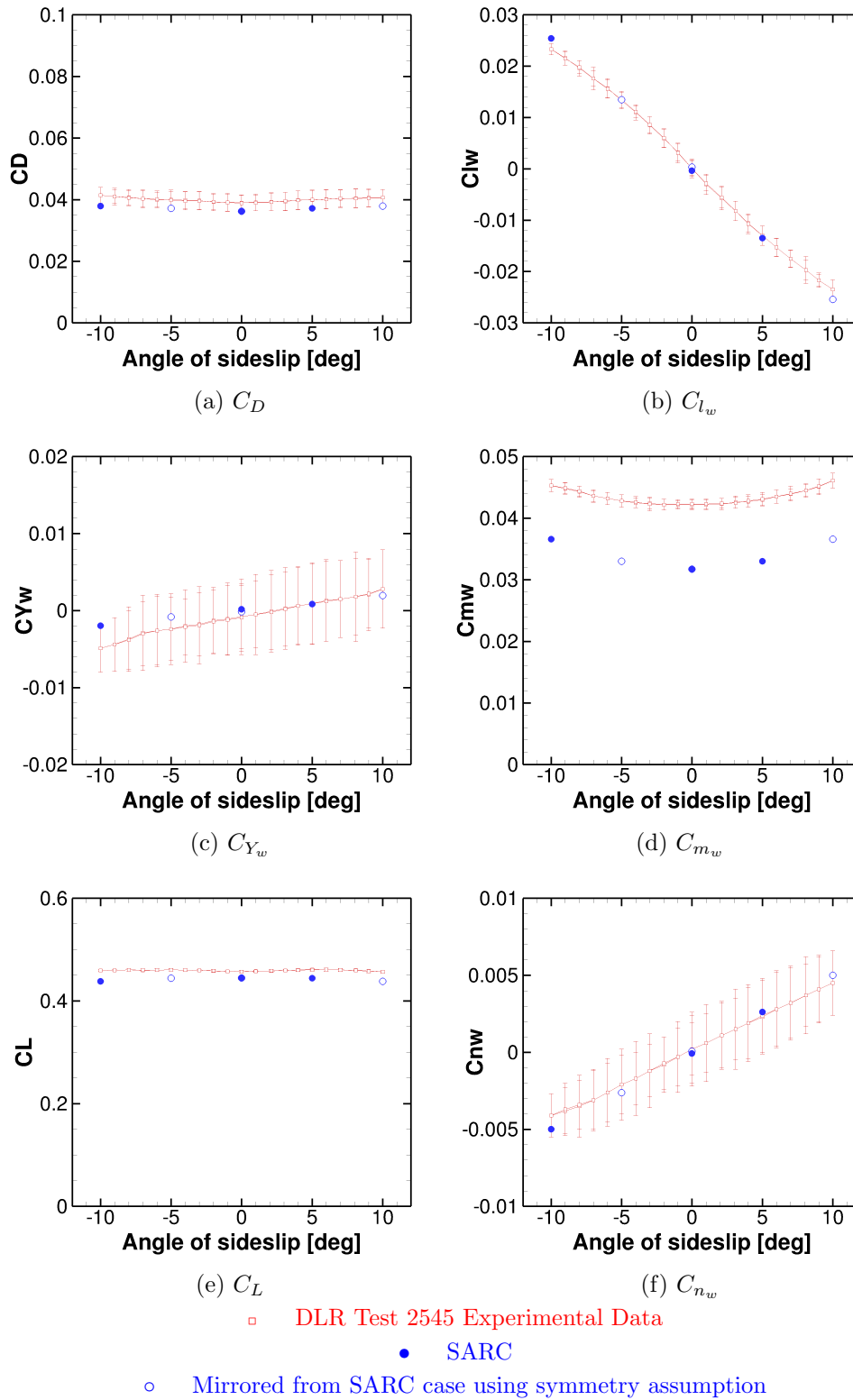


Figure 13. Force and moment coefficients for RN1007 (control surfaces undeflected, angle of sideslip sweep) cases.



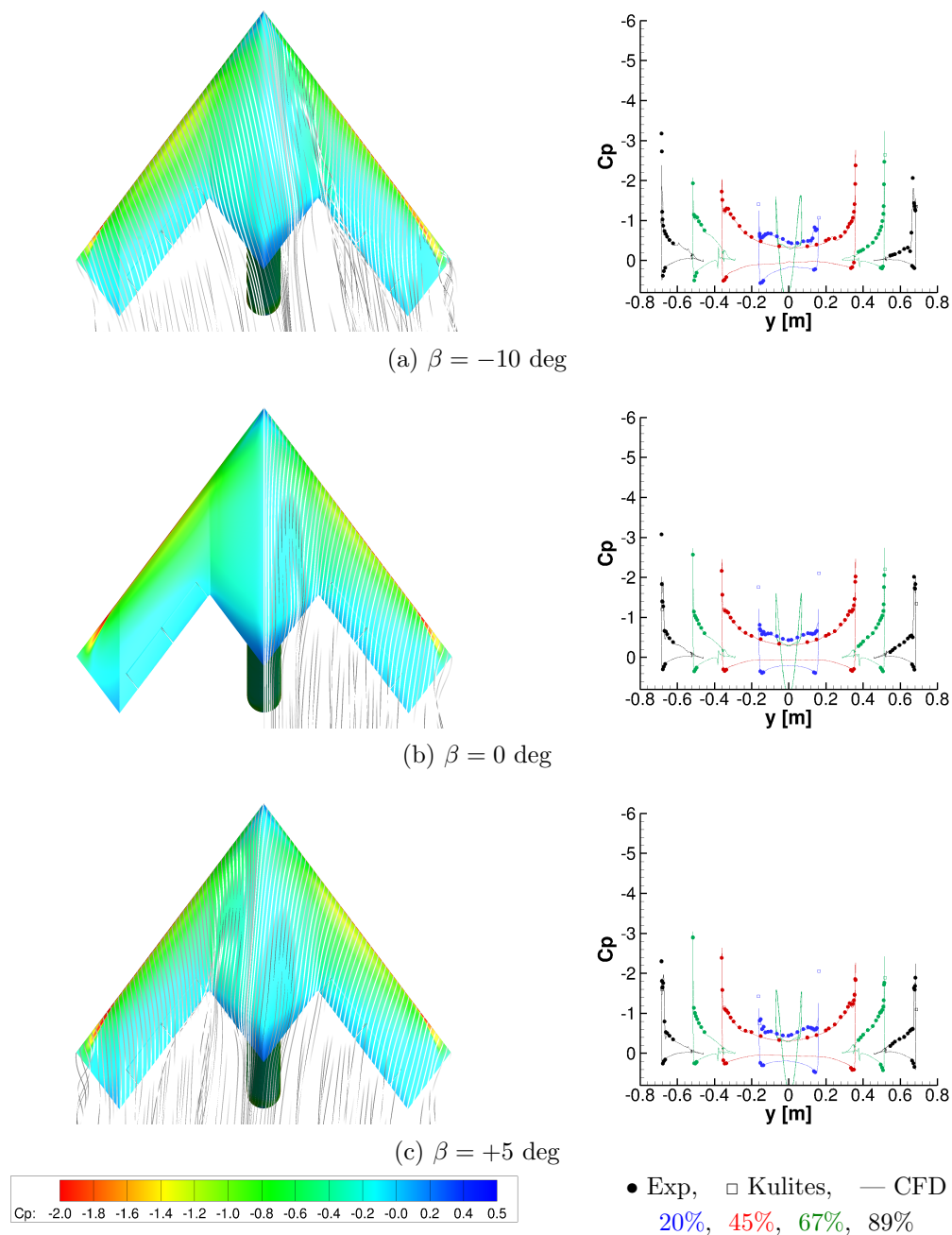


Figure 14. Pressure coefficients from the angle of sideslip sweep at an angle of attack of 10 degrees using the SARC turbulence model with no control surface deflections (RN1007).



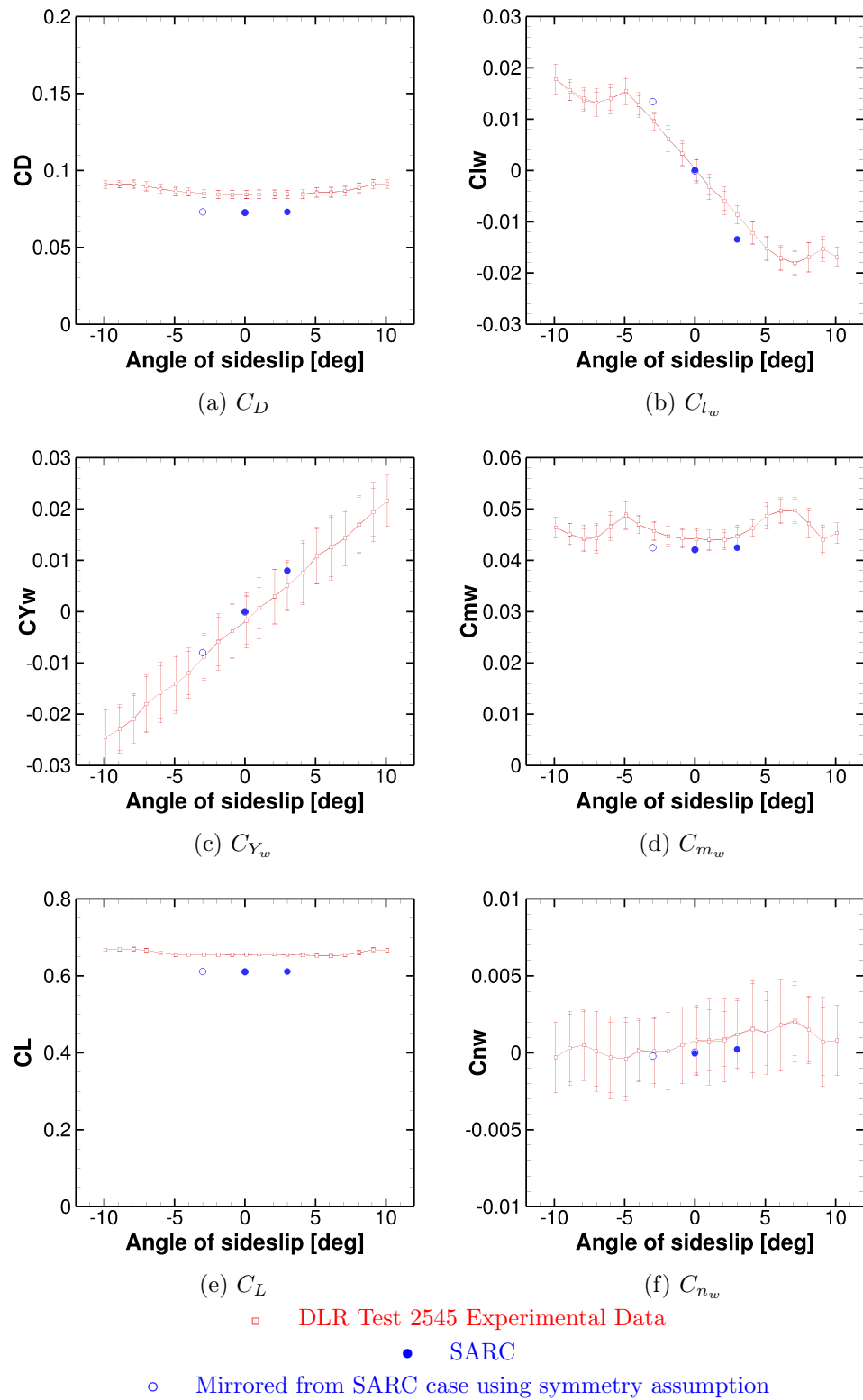


Figure 15. Force and moment coefficients for RN1008 (control surfaces undeflected, angle of sideslip sweep) cases.



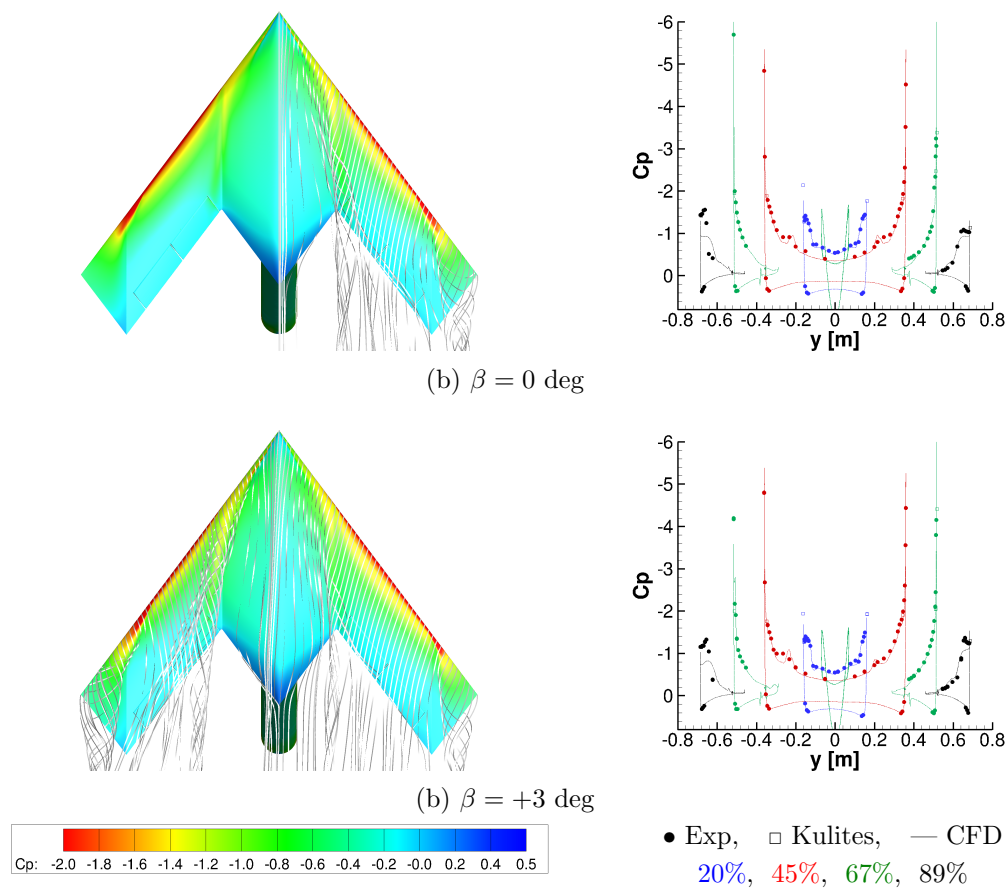


Figure 16. Pressure coefficients from the angle of sideslip sweep at an angle of attack of 10 degrees using the SARC turbulence model with no control surface deflections (RN1007).



change in mode from multiple leading edge vortices to one vortex located at the nose occurs over a smaller angle of attack range in the CFD than in the experiment. The lift coefficient is still underestimated at and above 20 degrees angle of attack. The effect of the control surface deflections on rolling moment coefficient is underestimated at angles of attack of 15 degrees and less. However, it does match the trends exhibited in the experimental data as it progresses through the pitch break from 16 to 18 degrees, and it is well matched at 20 and 25 degrees.

When looking at the plots comparing the pressure coefficients at the tap positions it is difficult to ascertain why there is such a mismatch in rolling moment coefficient. The asymmetry in the pressure field resulting from the control surface deflection appears to be well matched by the computational results. However, there are no pressure taps on the control surfaces themselves, so we do not know if any discrepancies exist on them. This is discussed further below where it is shown the difference between the overset and single grids has a marked effect on the rolling moment coefficient.

## IV.B. Dynamic Results

The dynamic cases presented some issues for the overset grid method as implemented in Cobalt. In brief, it meant that the overset grids could not be used to generate the force and moment data for dynamic cases. Therefore, in order to generate the pitch and yaw oscillation time histories, single (i.e. non overset) grids were used.

### IV.B.1. RN2342–50: Pitch Oscillation Around 10 Degrees at 1 Hz

Figure 19 presents the normal force coefficients for the single grid with different timesteps and turbulence models. One can see that they are practically overlayed on each other suggesting the timestep and turbulence model has very little impact on normal force for the pitching case. Figure 20 presents the pitching moment coefficient, showing the effect of timestep in the upper plot, and the effect of turbulence model in the lower plot.

Timestep convergence appears to have been achieved when comparing the  $\Delta t = 1 \times 10^{-4}$  and  $\Delta t = 5 \times 10^{-5}$  results. Although the  $\Delta t = 5 \times 10^{-5}$  case has not completed a full oscillation (this case had to be abbreviated due to re-prioritisation of computing resources) it does appear to closely track the  $\Delta t = 1 \times 10^{-4}$  results. There is a clear difference in the pitching moment behaviour with different timesteps. The larger timestep has the effect of making the oscillation appear as if it is happening at a higher frequency (i.e. a higher amplitude ‘ballooning’ of the phase plot).

If we refer to the experimental results for the pitch oscillation we can see that, at 1 Hz, the oscillation is slow enough that the pitching moment coefficient largely follows the trend of the static data. In particular, it matches the change in slope seen at around 11 or 12 degrees angle of attack. Despite the fact that the computational static data points are relatively scarce in the 5 to 15 degrees angle of attack range, it appears that the computational pitch oscillation also matches the changes in slope seen in the static *computational* data (refer to the green dashed line). It is just that the discrepancies in the static pitching moment coefficient mean that trying to computationally match the phase history of the experimental data is somewhat compromised to begin with.

### IV.B.2. RN2351–59: Pitch Oscillation Around 10 Degrees at 2 Hz

Figure 21a presents the normal force coefficient for the single grid with the SARC turbulence model. As per the 1 Hz case, the computational result is practically overlayed on the static data. Figure 21b presents the pitching moment coefficient result for the 2 Hz pitch oscillation. Again, the computational result is not particularly close to the experimental result. However, one can see that both computational and experimental show the higher amplitude ballooning of the pitching moment coefficient.

### IV.B.3. RN2270–78: Yaw Oscillation At 10 Degrees and 1 Hz

Figure 22 presents the body axis rolling and yawing moment coefficients for the single grid during the yaw oscillation,  $\psi = \pm 5$  degrees at a pitch angle of 10 degrees. Timestep convergence was not repeated for the yaw cases, therefore the converged timestep for the pitch oscillation of  $1 \times 10^{-4}$  was used.

It can be seen in figure 22 that, for reasons unknown, the signal is extremely noisy.



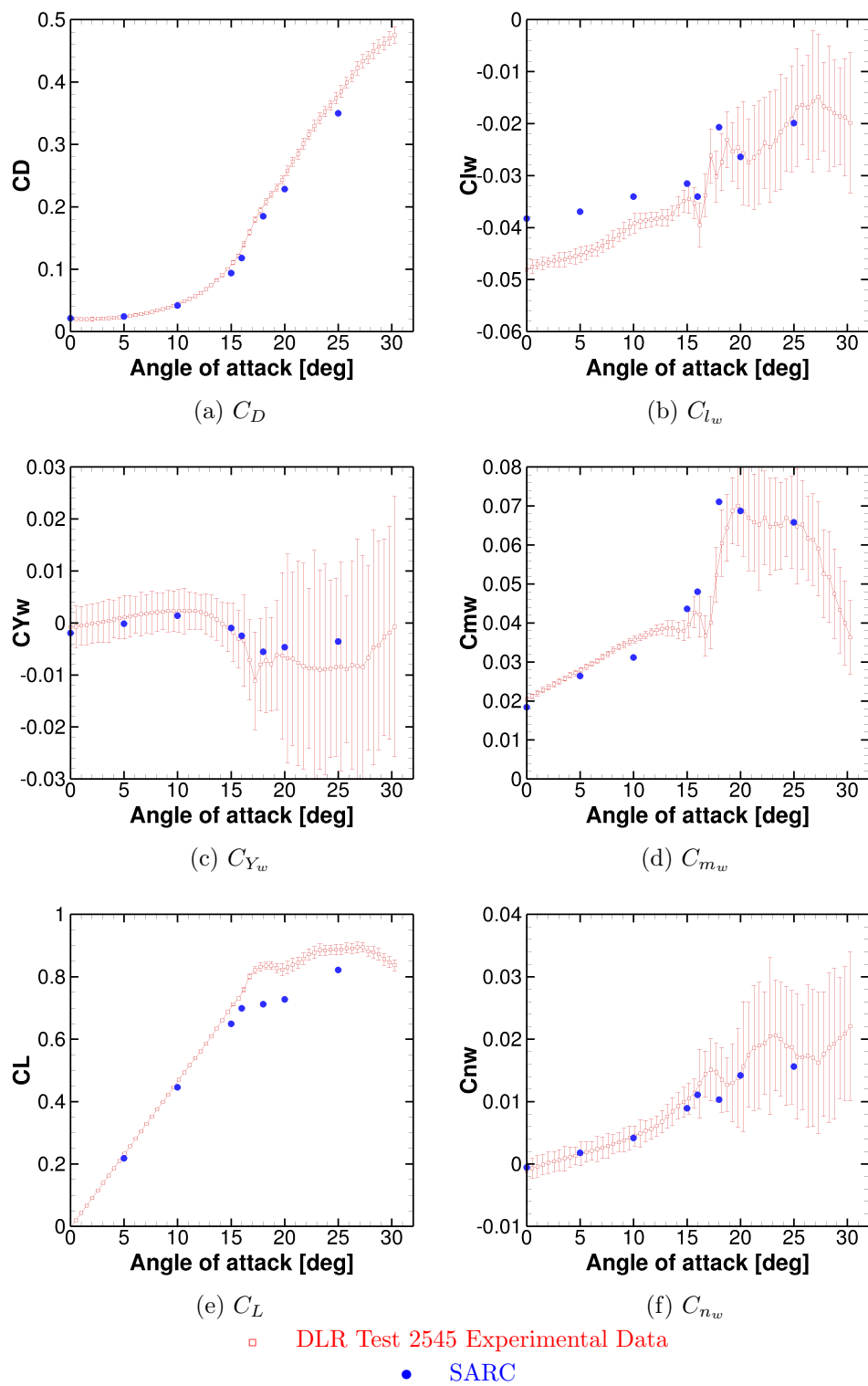


Figure 17. Force and moment coefficients for RN1103 (control surfaces fully deflected, angle of attack sweep) case.



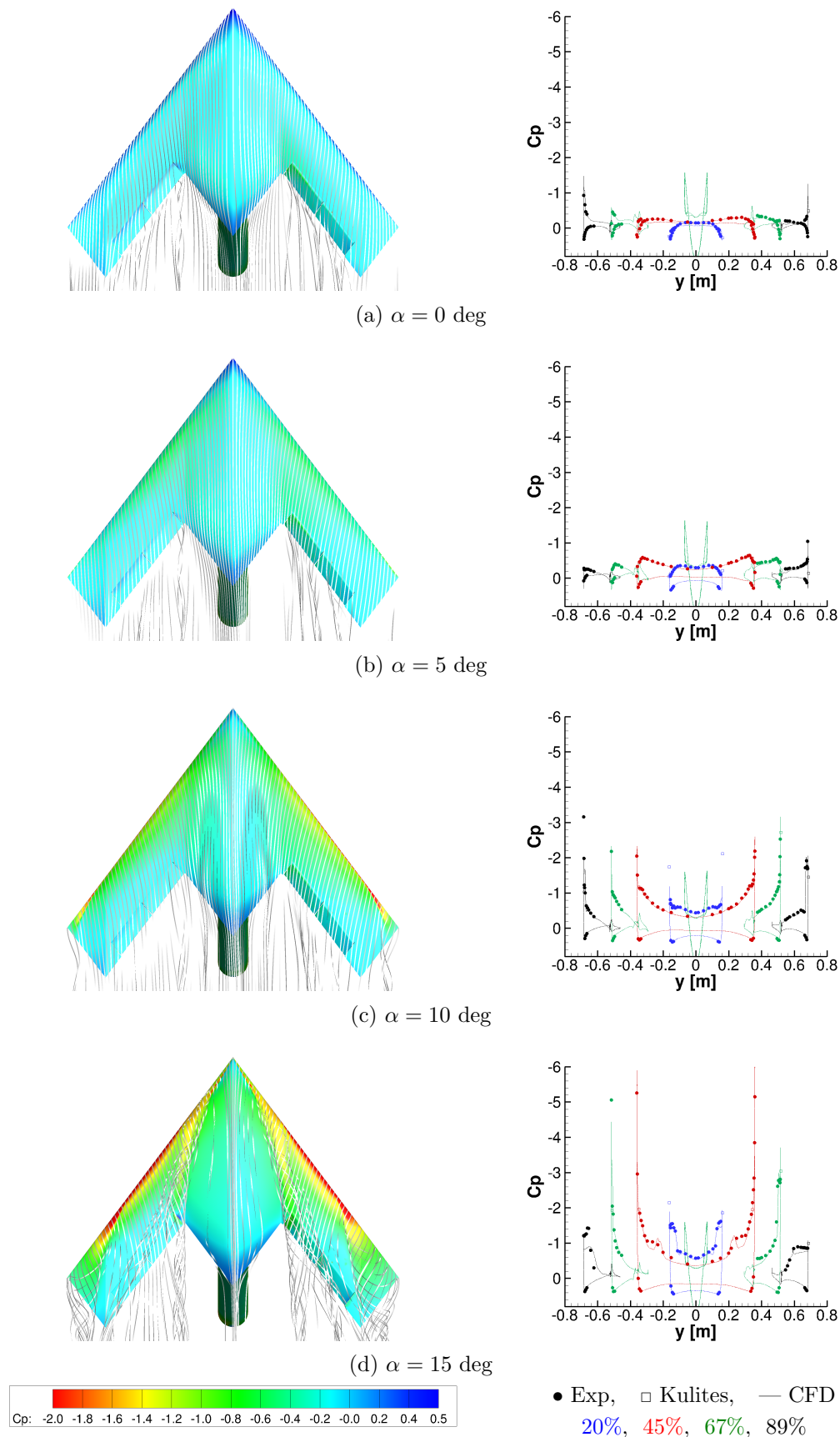
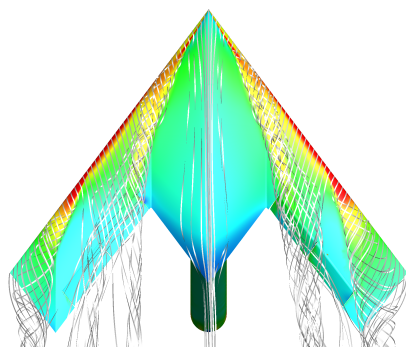
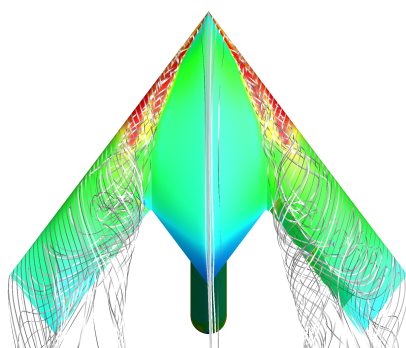
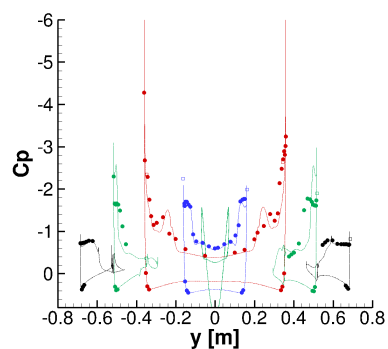


Figure 18. Pressure coefficients from the angle of attack sweep using the SARC turbulence model with control surface deflections for maximum roll moment (RN1103).

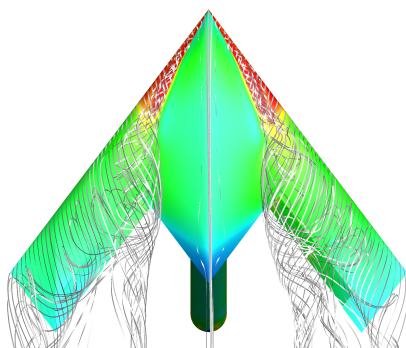
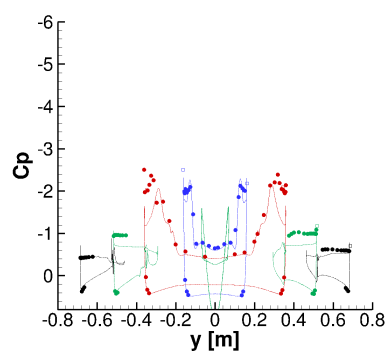




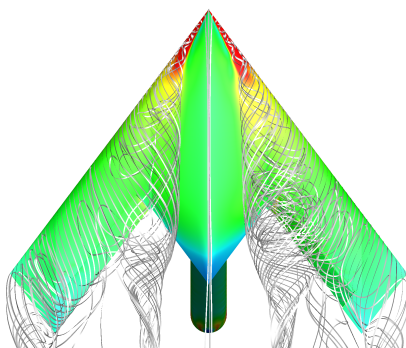
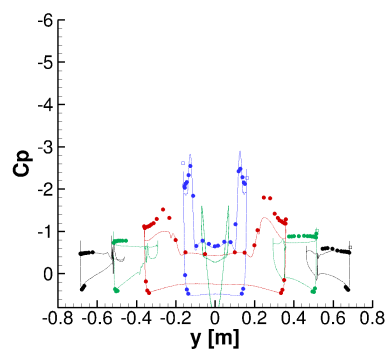
(e)  $\alpha = 16$  deg



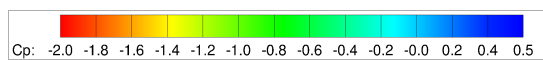
(f)  $\alpha = 18$  deg



(g)  $\alpha = 20$  deg



(h)  $\alpha = 25$  deg



• Exp, □ Kulites, — CFD  
20%, 45%, 67%, 89%



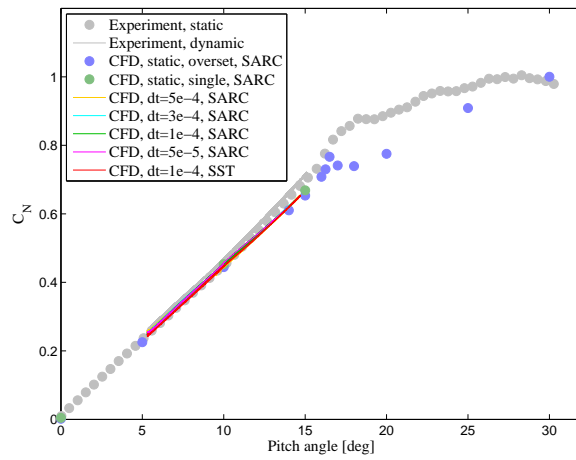


Figure 19. Normal force coefficient results for the dynamic pitch about 10 degrees angle of attack at 1 Hz.

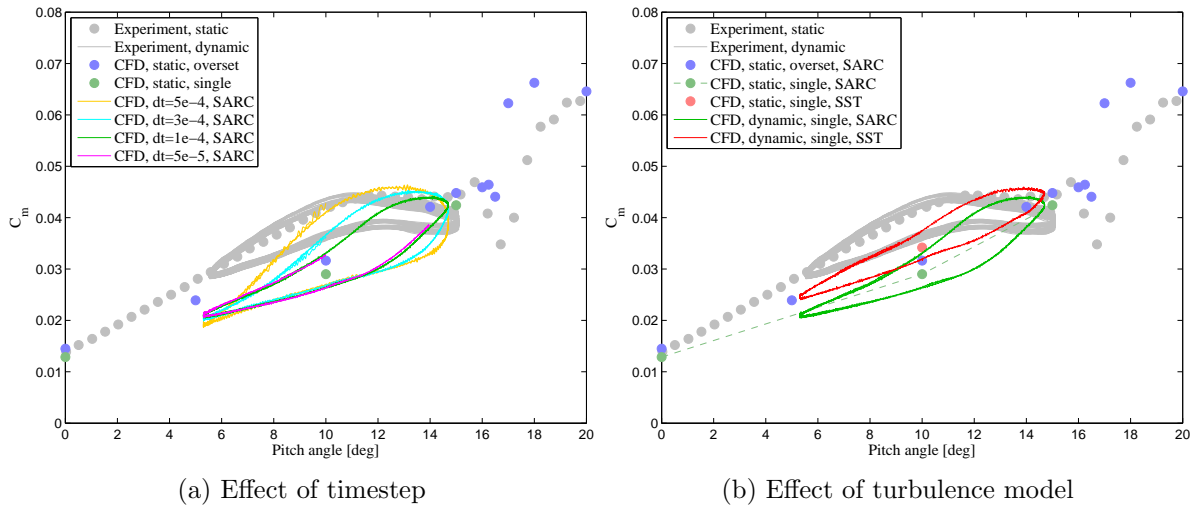


Figure 20. Pitching moment coefficient results for the dynamic pitch about 10 degrees angle of attack at 1 Hz.

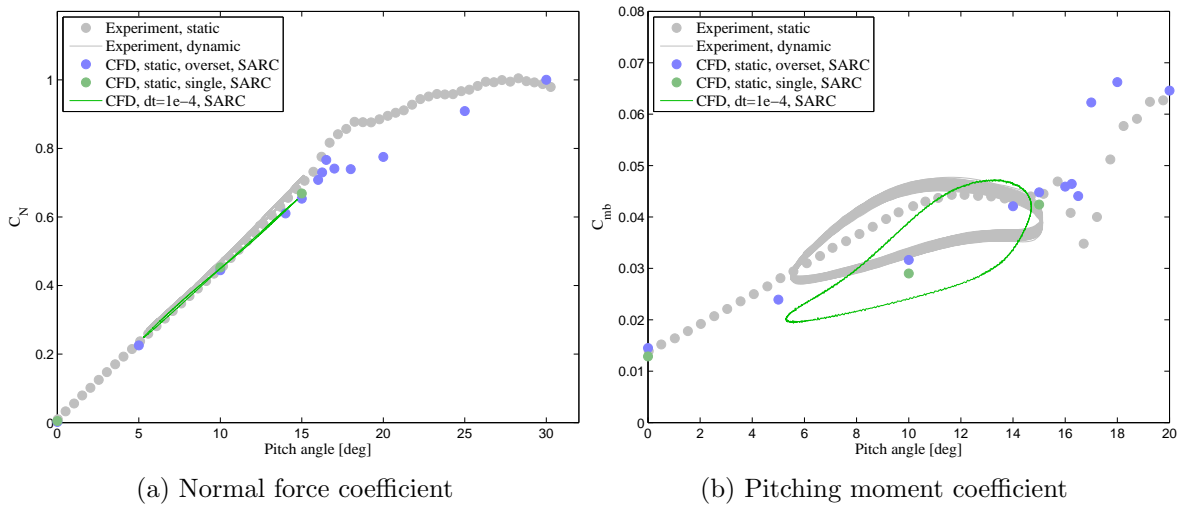


Figure 21. Results for the dynamic pitch about 10 degrees angle of attack at 2 Hz.



The rolling moment coefficient matches the experimental data relatively closely, but with a slightly larger slope. The yawing moment coefficient matches in broad terms of the slope relative to the yaw angle; however, the large noise levels on the signal mean that the clear phase loop that is evident in the experimental data is not evident in the computational results.

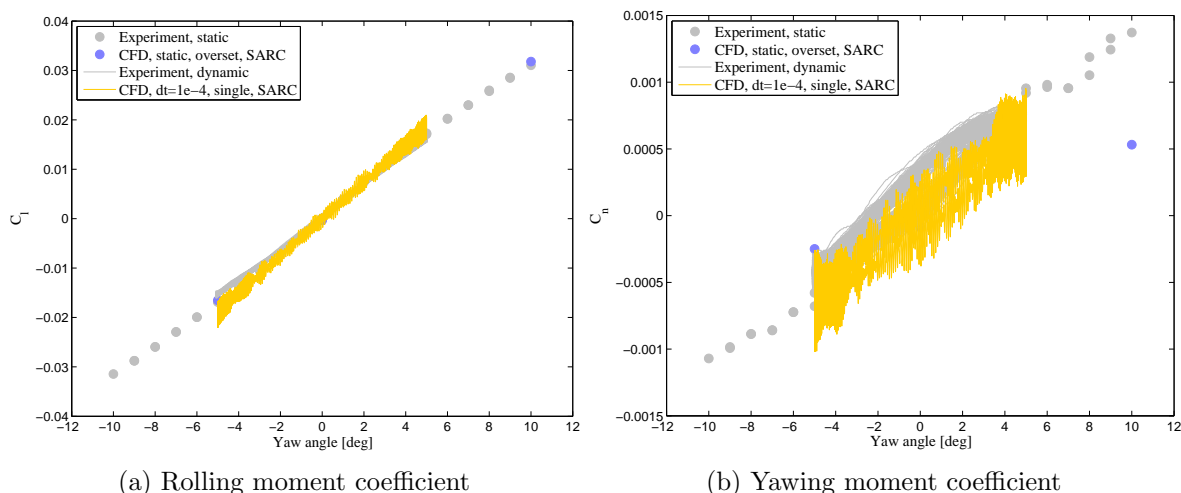


Figure 22. Results for the dynamic yaw of  $\pm 5$  degrees at 10 degrees angle of attack at 1 Hz.

#### IV.C. Effect of Overset Grid

In order to establish the effect of the overset grid—including the control surface gaps and differences in geometry—two ‘single’ grids were also created (one for zero deflections, one for full maximum roll deflections). These single grids maintained, as much as possible, the same mesh distribution on the surface and similar density around the aircraft and control surfaces. Therefore, in the undeflected case (where the geometry differences were minimal), notwithstanding the effects of the hole-cut algorithm for the overset grid, it is likely that any differences between the two results are attributable to the existence of the gap. For the deflected case, both the presence of the gap and the differences in geometry may contribute to any differences.

Figure 23 shows the difference between the lift and pitching moment coefficients for the full-span overset grid compared with the half-span single grid for the case where the control surfaces are undeflected (RN1001). The pitching moment coefficient at an angle of attack of 10 degrees is 8% lower for the single grid than for the overset grid when using the SARC turbulence model, and similar differences arise for the SST model. The pitching moment coefficient for the single grid at the other two points sampled—angles of attack of 0 and 15 degrees—is also lower than the overset grid, but to a lesser extent. Figure 24 shows the difference between the rolling moment coefficients for the overset grid compared with the single grid for the case where the port control surfaces are deflected  $-20$  degrees and the starboard control surfaces are deflected  $+20$  degrees (RN1103). At zero angle of attack the overset grid underestimates the experimental data by 20% and underestimates the single grid result by 26%. It is not clear whether the major contribution to the difference in rolling moment coefficient is due to the presence of the gap itself, or due to the differences in geometry. There is also an increase in drag of approximately 14 drag counts for the overset grid at zero degrees angle of attack in both the undeflected and deflected cases. We shall compare the flowfields for the two cases and identify some of the differences.

Figures 25 and 26 show streamlines interacting with the control surface gap as it exists in the overset mesh for different angles of attack and control surface deflections. The streamlines are coloured according to velocity magnitude (in  $\text{m s}^{-1}$ ).

Figure 25 shows the starboard wing (pictured from behind and below the wing) with control surfaces undeflected, at angles of attack of 0 and 15 degrees. For the  $\alpha = 0$  case, streamlines can be seen flowing along the underside of the wing before becoming momentarily entrained in the chordwise control surface gap. It can be seen that some of the streamlines slow upon interaction with the gap. For the  $\alpha = 15$  case, some of the streamlines travelling along with underside of the wing can be seen disappearing into the chordwise control surface gaps.



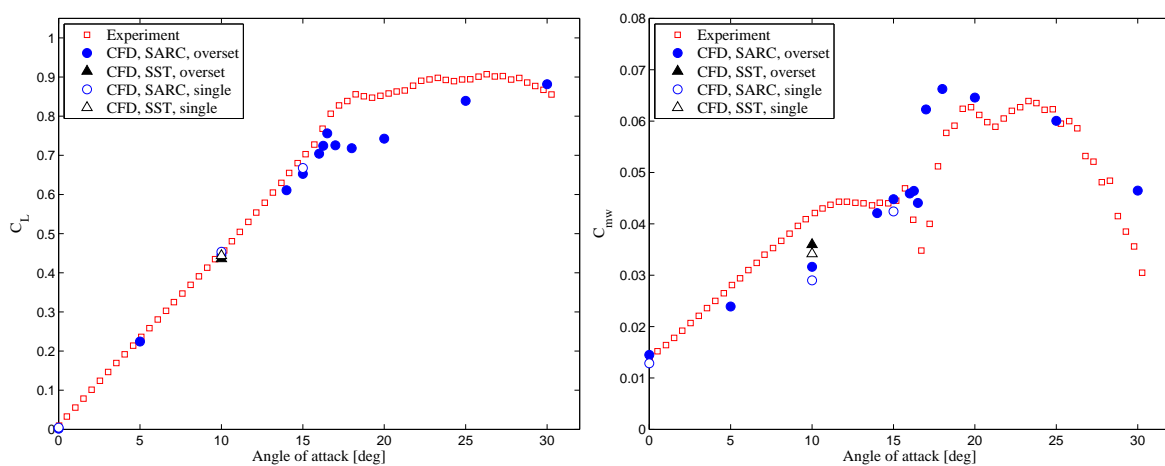


Figure 23. Comparing overset grid results with results for a single grid for the RN1001 case with control surfaces undeflected.

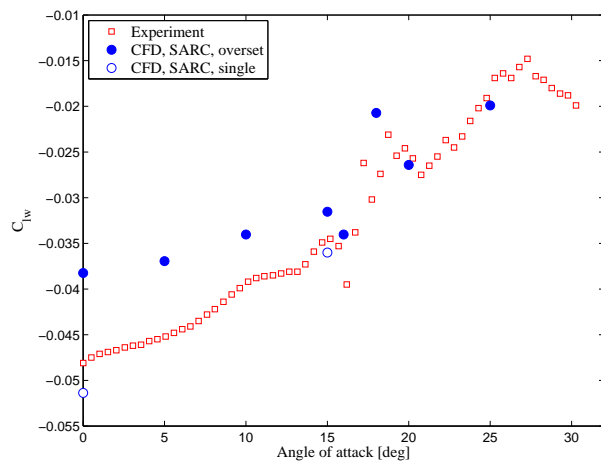


Figure 24. Comparing overset grid results with results for a single grid for the RN1103 case with control surfaces deflected: port wing  $-20$  degrees, starboard wing  $+20$  degrees.

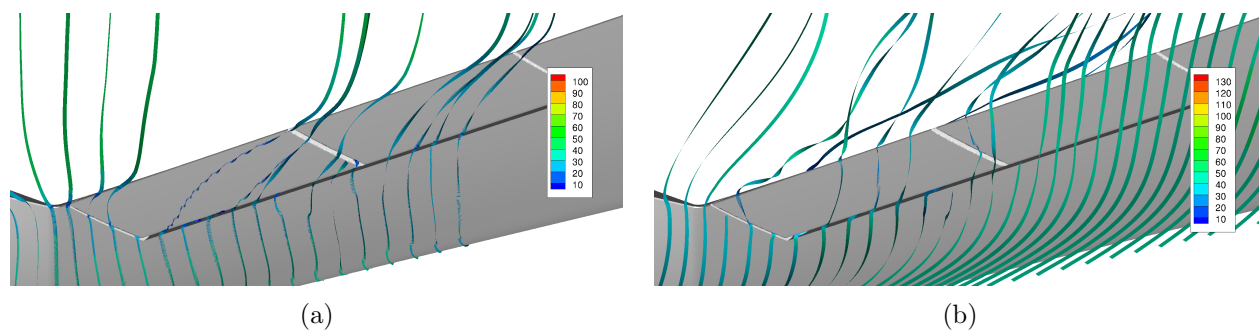
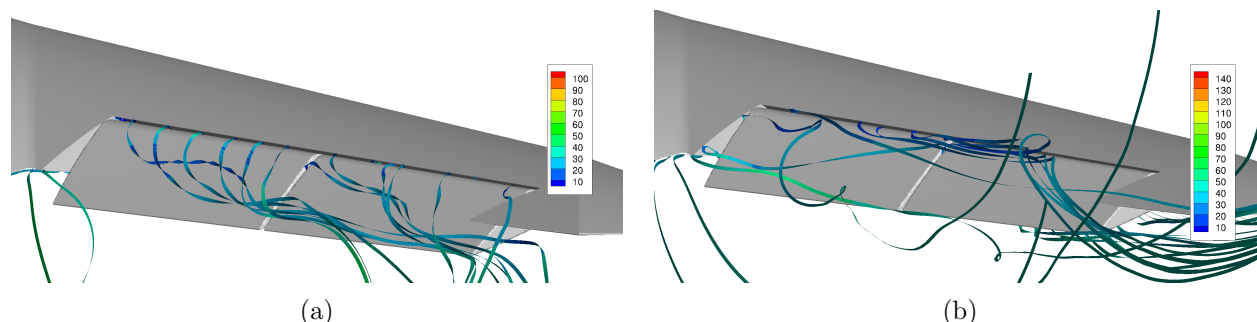


Figure 25. Starboard wing with control surfaces undeflected showing streamlines interacting with the control surface gaps: (a)  $\alpha = 0$  degrees, (b)  $\alpha = 15$  degrees (view is from behind and below the wing).



Figure 26 shows the starboard wing (pictured from behind and above the wing) with control surfaces deflected +20 degrees, at angles of attack of 0 and 15 degrees. For the  $\alpha = 0$  case, streamlines can be seen coming through both the chordwise and streamwise gaps from the underside of the wing. For the  $\alpha = 15$  case, streamlines can again be seen coming through the chordwise gaps from the underside of the wing.



**Figure 26. Starboard wing with control surfaces deflected at +20 degrees showing streamlines coming through the control surface gaps at (a)  $\alpha = 0$  degrees and (b)  $\alpha = 15$  degrees (view is from behind and above the wing).**

Figures 27a and b show slices through the wing at  $y = 0.35$  m for an angle of attack of 0 degrees, comparing the contours of velocity magnitude between the overset and single grid, respectively. The velocity magnitude within the overset grid gap is very small (less than  $10 \text{ m s}^{-1}$ ), and the gap does not appear to have any great effect on the flow outside of the gap, aside from possibly thickening the boundary layer. Contrast this to figure 27c, which also shows a slice through the wing at  $y = 0.35$  m, but for an angle of attack of 15 degrees. The velocity in the gap is around  $20$  to  $30 \text{ m s}^{-1}$  and the gap appears to be contributing to the low-speed air over the upper surface of the control surface that is clearly not evident in the single grid (figure 27d).

Figures 28a to d show the spanwise slices at  $y = \pm 0.35$  m with control surfaces deflected  $\pm 20$  degrees at zero degrees angle of attack. Figures 28e to h show the same slices and deflections at an angle of attack of 15 degrees. At zero degrees angle of attack (figures 28a to d), both the positive and negative control surface deflections show similar, albeit inverted, flowfields. The velocity inside the gap is around  $20$  to  $30 \text{ m s}^{-1}$ , and there is a larger region of low speed air in the wake of the deflected control surface for the overset grid than for the single grid. For an angle of attack of 15 degrees, the positive and negative deflections result in different flowfields. In figure 28e, showing a positive control surface deflection, the flow in the gap is around  $30$  to  $40 \text{ m s}^{-1}$  and it would appear that the lower velocity fluid, possibly emanating from the gap, is finding its way into the freestream when compared to the single grid. However, there are no significant differences apparent when comparing the  $-20$  degree deflection cases at  $\alpha = 15$  degrees as shown in figures 28g and h. This can possibly explain some of the differences in the rolling moment coefficient observed between the overset and single grids, where the most significant difference was seen at  $\alpha = 0$  degrees, and at  $\alpha = 15$  degrees, the discrepancy had reduced considerably.

The velocity fields shown in figure 28 do not fully convey the significant difference in the flowfield when compared with the pressure field shown in figure 29, which shows the contours of pressure coefficient at a cut through the starboard wing at zero angle of attack for the flaps deflected in the maximum roll configuration. Comparing the images in figures 29a and 29b it can be seen that the single grid has a much higher suction on the upper surface. This explains the very different roll moment effectiveness seen for this case in figure 24. It can be seen that the peak in the suction pressure for the single grid occurs close to the position of the gap in the overset grid. It appears that the combination of the gap and geometry differences interrupt the build up of the suction on the upper surface in the overset case.

Figure 30 compares the surface pressure coefficient close to the control surfaces for the overset and single grids at an angle of attack of 10 degrees using the SARC turbulence model. The maximum and minimum of the contours of pressure coefficient are limited so as to highlight the flow features near the control surfaces. Clearly the contours are much smoother for the single grid shown on the right. The overset results shown on the left show some disturbance in the flowfield. It is not known if this is purely attributable to the presence of the gap, or possibly also due to the hole-cut algorithms associated with the overset method. It is suggested that where there is blotchiness, such as just upstream of the outboard edge of the outboard control surface, this may be attributable to the overset algorithm. And where there is a ‘smooth’ difference between the



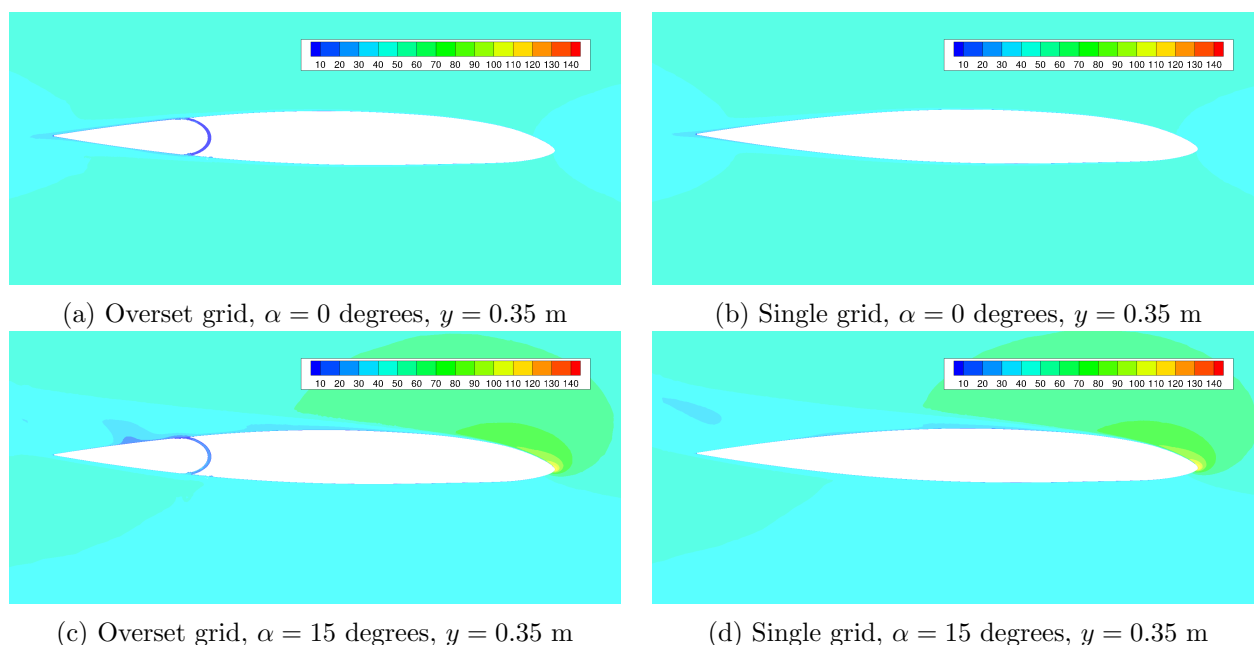


**Figure 27. Comparing flowfield velocity magnitudes at slices through wing for overset and single grids with control surfaces undeflected. Contours are velocity magnitude in  $\text{m s}^{-1}$ .**

overset and single grids, such as the mismatch in pressure coefficient either side of the inboard-most spanwise gap, this is attributable to the presence of a gap. Note that the apparent difference in the chordwise size of the control surfaces is due to the issues discussed in section III.B and shown in figures 4 and 5.

## V. Conclusion

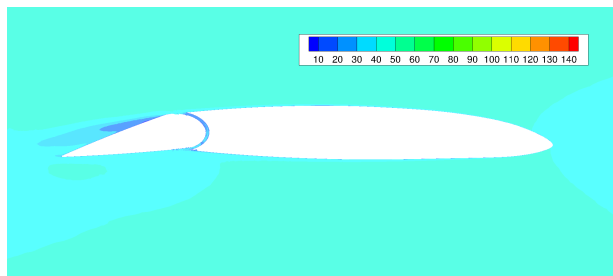
The Cobalt CFD code was used with an overset grid in order to generate static and dynamic force, moment and pressure coefficients for comparison with wind tunnel tests. The overset grid was used to ease meshing requirements for the cases with deflected control surfaces, and in anticipation of use of the model with reduced-order models that require the dynamic deflection of the control surface. The primary turbulence model tested was SARC, which was shown to give a reasonable overall match in force, moment and surface pressure coefficients for the angle of attack sweeps both with and without control deflections. However, there were areas of notable discrepancies: the slope of the pitching moment coefficient against angle of attack below an angle of attack of 15 degrees is less than the experimental data. The pitch break occurring around 16 degrees angle of attack is not as significant and appears to occur over a smaller angle of attack range than in experiment. And the lift coefficient initially reduces above the stall before recovering, unlike the behaviour seen in experiment.

Limited testing was performed on alternative turbulence models, and it was found that they offered some improvement in the pitching moment slope. However, the differences in these turbulence models was not consistent, therefore it was not clear what particular phenomena was being resolved and therefore leading to the improved results.

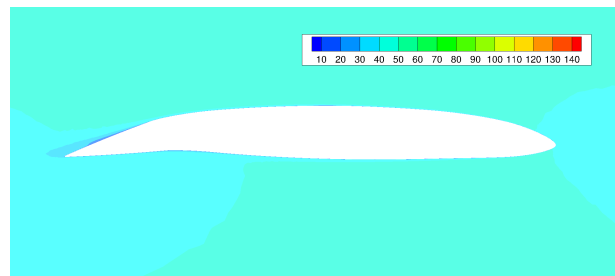
Dynamic pitch and yaw oscillations were also tested. For the pitch oscillations, it was shown that the discrepancies in the static pitching moment coefficient were reflected in the dynamic tests and they were therefore quite different to the experimental results. The dynamic yaw oscillations exhibited a high level of noise in the force and moment results, but matched experimental data well.

Finally, the overset grid was compared to single grids with and without control deflections to identify the effect of the geometry changes and chordwise gap introduced by the use of the overset method. It was found that the gap likely does affect the results. There was not a significant effect on the normal force coefficient; however, the pitching moment coefficient at an angle of attack of 10 degrees was around 8% less for the single grid than for the overset grid. There was also a significant difference in rolling moment coefficient between the single and overset grids at an angle of attack of 0 degrees, which is probably attributable to the combined effects of the geometry differences and the gap. Finally, it was also shown that the modifications to the geometry for the overset grid influenced the flowfield in the region of the control surfaces.

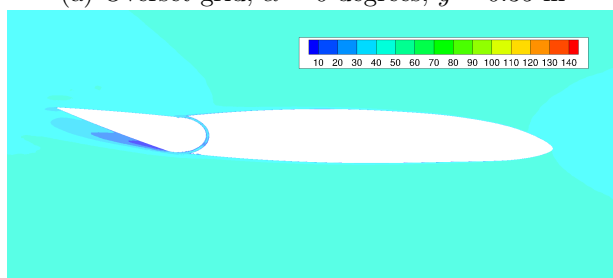




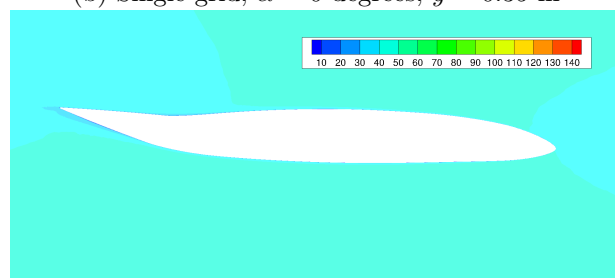
(a) Overset grid,  $\alpha = 0$  degrees,  $y = 0.35$  m



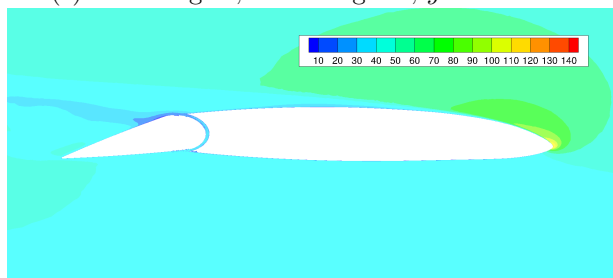
(b) Single grid,  $\alpha = 0$  degrees,  $y = 0.35$  m



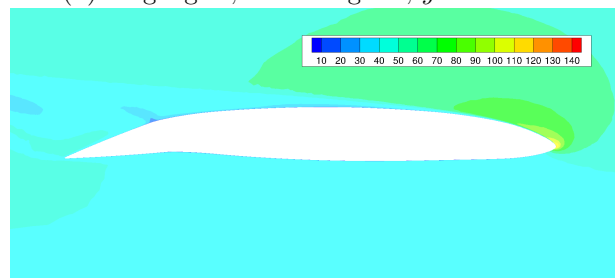
(c) Overset grid,  $\alpha = 0$  degrees,  $y = -0.35$  m



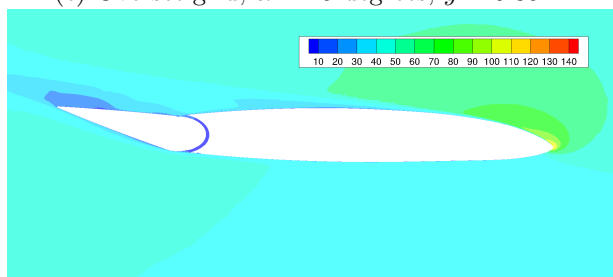
(d) Single grid,  $\alpha = 0$  degrees,  $y = -0.35$  m



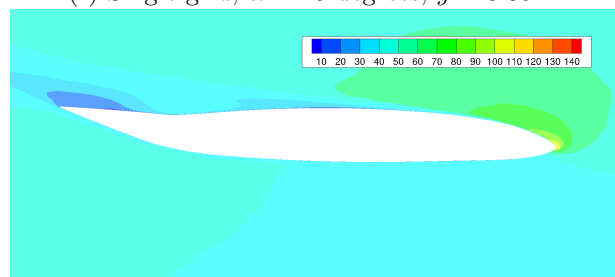
(e) Overset grid,  $\alpha = 15$  degrees,  $y = 0.35$  m



(f) Single grid,  $\alpha = 15$  degrees,  $y = 0.35$  m



(g) Overset grid,  $\alpha = 15$  degrees,  $y = -0.35$  m



(h) Single grid,  $\alpha = 15$  degrees,  $y = -0.35$  m

**Figure 28.** Comparing flowfield velocity magnitudes at slices through wing for overset and single grids with control surfaces deflected. Contours are velocity magnitude in  $\text{m s}^{-1}$ .



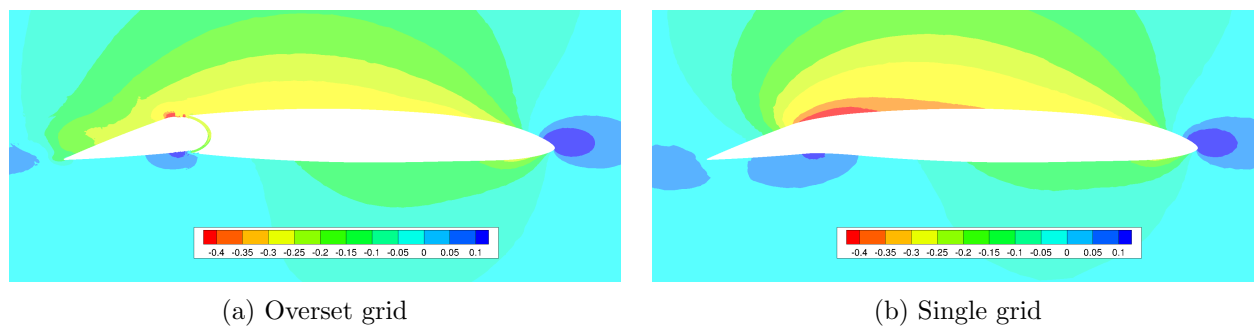


Figure 29. Comparing contours of pressure coefficient at slices through wing at  $y = 0.35$  m and  $\alpha = 0$  degrees for overset and single grids with control surfaces deflected.

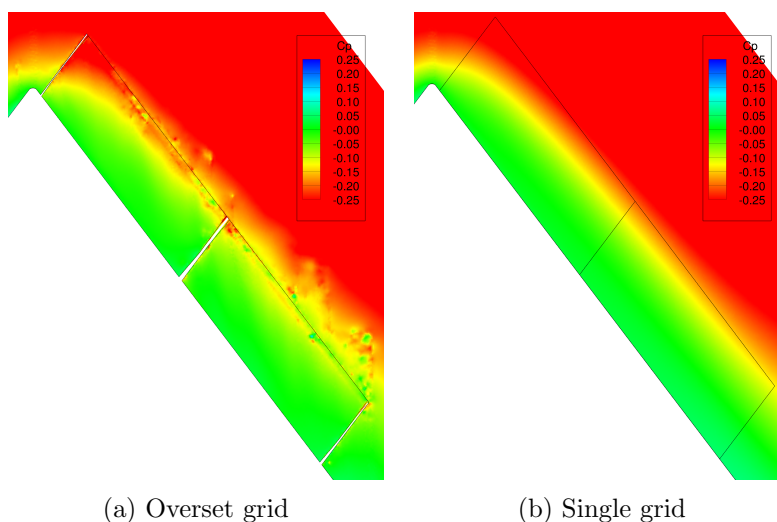


Figure 30. Detail of the control surfaces showing contours of pressure coefficient for the (a) overset and (b) single grids using SARC turbulence model at 10 degrees angle of attack.



## Acknowledgments

Computational resources for this project were provided by the HPC centres at the Engineering Research and Development Center, Vicksburg, Mississippi and at the Air Force Research Laboratory, Wright-Patterson Air Force Base, Ohio through the US Department of Defense's High Performance Computing Modernization Program.

Thanks to the High Performance Computing Research Center at the U.S. Air Force Academy who hosted the first author as part of the Engineer and Scientist Exchange Program.

Thanks to the other members of the NATO AVT-201 Panel for their questions, answers, and insights that have helped progress this work.

Thanks also to Ken Wurtzler and Bob Tomaro of Cobalt Solutions LLC, who provided comment, guidance, and troubleshooting on various aspects of using the overset method in Cobalt.

## References

- <sup>1</sup>Cummings, R. and Schütte, A., "The NATO STO Task Group AVT-201 on Extended Assessment of Stability and Control Prediction Methods for NATO Air Vehicles," *32nd AIAA Applied Aerodynamics Conference*, Atlanta, Georgia, 2014, AIAA-2014-2000.
- <sup>2</sup>Liersch, C. and Huber, K., "Conceptual design and aerodynamic analyses of a generic UCAV configuration," *32nd AIAA Applied Aerodynamics Conference*, Atlanta, Georgia, 2014, AIAA-2014-2001.
- <sup>3</sup>Huber, K., Vicroy, D., Schütte, A., and Hübner, A., "UCAV model design and static experimental investigations to estimate control device effectiveness and S&C capabilities," *32nd AIAA Applied Aerodynamics Conference*, Atlanta, Georgia, 2014, AIAA-2014-2002.
- <sup>4</sup>Tormalm, M. and Schmidt, S., "Computational study of static and dynamic vortical flow over the delta wing SACCON configuration using the FOI flow solver Edge," *28th AIAA Applied Aerodynamics Conference*, Chicago, Illinois, 2010, AIAA-2010-4561.
- <sup>5</sup>LeRoy, J.-F. and Morgand, S., "SACCON CFD static and dynamic derivatives using ElsA," *28th AIAA Applied Aerodynamic Conference*, Chicago, Illinois, 2010, AIAA-2010-4562.
- <sup>6</sup>Cummings, R., Jirasek, A., Petterson, K., and Schmidt, S., "SACCON static and dynamic motion flow physics simulation using Cobalt," *28th AIAA Applied Aerodynamics Conference*, Chicago, Illinois, 2010, AIAA-2010-4691.
- <sup>7</sup>Schütte, A., Hummel, D., and Hitzel, S., "Numerical and experimental analyses of the vortical flow around the SACCON configuration," *28th AIAA Applied Aerodynamics Conference*, Chicago, Illinois, 2010, AIAA-2010-4690.
- <sup>8</sup>Frink, N., "Strategy for dynamic CFD simulations on SACCON configuration," *28th AIAA Applied Aerodynamics Conference*, Chicago, Illinois, 2010, AIAA-2010-4559.
- <sup>9</sup>Chi, D., Chakravarthy, S., and Goldberg, U., "Flow prediction around the SACCON configuration using CFD++," *28th AIAA Applied Aerodynamics Conference*, Chicago, Illinois, 2010, AIAA-2010-4563.
- <sup>10</sup>Cummings, R. and Schütte, A., "Integrated computational/experimental approach to unmanned combat air vehicle stability and control estimation," *J. Aircraft*, Vol. 49, 2012, pp. 1542–1557.
- <sup>11</sup>Vicroy, D., Huber, K., Loeser, T., and Rohlf, D., "Low-speed dynamic wind tunnel test analysis of a generic 53 swept UCAV configuration," *32nd AIAA Applied Aerodynamics Conference*, Atlanta, Georgia, 2014, AIAA-2014-2003.
- <sup>12</sup>Cobalt Solutions, *Cobalt User's Manual Version 6.0*, Cobalt Solutions LLC, Springfield, 2013.
- <sup>13</sup>Strang, W., Tomaro, R., and Grismer, M., "The defining methods of Cobalt60: A parallel, implicit, unstructured Euler/Navier-Stokes flow solver," *37th AIAA Aerospace Sciences Meeting and Exhibit*, Reno, Nevada, 1999, AIAA-1999-0786.
- <sup>14</sup>Gottlieb, J. and Groth, C., "Assessment of Riemann solvers for unsteady one-dimensional inviscid flows of perfect gases," *J. Fluids and Structures*, Vol. 78, No. 2, 1998, pp. 437–458.
- <sup>15</sup>Tomaro, R., Strang, W., and Sankar, L., "An implicit algorithm for solving time dependent flows on unstructured grids," 1997, AIAA-1997-0333.
- <sup>16</sup>Spalart, P. and Allmaras, S., "A one equation turbulence model for aerodynamic flows," 1992, AIAA-1992-0439.
- <sup>17</sup>Spalart, P. R. and Shur, M. L., "On the sensitization of turbulence models to rotation and curvature," *Aerospace Sci. Tech.*, Vol. 1, 1997, pp. 297–302.
- <sup>18</sup>Wilcox, D., "Reassessment of the scale determining equation for advanced turbulence models," *AIAA Journal*, Vol. 26, 1988, pp. 1299–1310.
- <sup>19</sup>Menter, F., "Eddy viscosity transport equations and their relation to the  $k-\epsilon$  model," *ASME Journal of Fluids Engineering*, Vol. 119, 1997, pp. 876–884.
- <sup>20</sup>Schütte, A., Huber, K., and Boelens, O., "Static and dynamic numerical simulations of a generic UCAV configuration with and without control devices," *32nd AIAA Applied Aerodynamics Conference*, Atlanta, Georgia, 2014, AIAA-2014-2132.
- <sup>21</sup>Frink, N., "Stability and control CFD investigations of a generic 53-deg swept UCAV configuration," *32nd AIAA Applied Aerodynamics Conference*, Atlanta, Georgia, 2014, AIAA-2014-2133.
- <sup>22</sup>Kennett, D., Hoholis, G., and Badcock, K., "Numerical simulation of control surface deflections over a generic UCAV configuration at off-design flow conditions," *32nd AIAA Applied Aerodynamics Conference*, Atlanta, Georgia, 2014, AIAA-2014-2134.
- <sup>23</sup>Coppin, J. and Birch, T., "CFD predictions of control effectiveness for a generic highly swept UCAV configuration," *32nd AIAA Applied Aerodynamics Conference*, Atlanta, Georgia, 2014, AIAA-2014-2135.



- <sup>24</sup>Lofthouse, A., Ghoreyshi, M., Cummings, R., and Young, M., "Static and dynamic simulations of a generic UCAV geometry using the Kestrel flow solver," *32nd AIAA Applied Aerodynamics Conference*, Atlanta, Georgia, 2014, AIAA-2014-2264.
- <sup>25</sup>LeRoy, J.-F., Morgand, S., and Farcy, D., "Static and dynamic derivatives on generic UCAV without and with leading edge control," *32nd AIAA Applied Aerodynamic Conference*, Atlanta, Georgia, 2014, AIAA-2014-2391.
- <sup>26</sup>Tomac, M. and Tormalm, M., "Stability and control assessment of a generic UCAV design using the Edge flow solver," *32nd AIAA Applied Aerodynamics Conference*, Atlanta, Georgia, 2014, AIAA-2014-2392.
- <sup>27</sup>Ghoreyshi, M., Young, M., Jirásek, A., Lofthouse, A., and Cummings, R., "Validation of unsteady aerodynamic models of a generic UCAV using overset grids," *32nd AIAA Applied Aerodynamics Conference*, AIAA, Atlanta, Georgia, 2014, AIAA-2014-2265.
- <sup>28</sup>Ghoreyshi, M., Jirásek, A., Cummings, R., Tomaro, R., and Wurtzler, K., "Static and dynamic loads modeling of an aerodynamic control surface," *51st AIAA Aerospace Sciences Meeting*, AIAA, Grapevine, Texas, 2013, AIAA-2013-0664.
- <sup>29</sup>Young, M., Ghoreyshi, M., Lofthouse, A., and Cummings, R., "Investigating mesh quality on overset gridding of a flapped aerofoil," to be presented at 19th Australasian Fluid Mechanics Conference.
- <sup>30</sup>Tyssel, L., "Hybrid grid generation for complex 3D geometries," *7th International Conference on Numerical Grid Generation in Computational Fluid Simulation*, 2000, pp. 337–346.
- <sup>31</sup>Tyssel, L., "The TRITET Grid Generation System," *10th International Conference on Numerical Grid Generation in Computational Field Simulations*, 2007.
- <sup>32</sup>Jirásek, A., Cummings, R., Schütte, A., and Huber, K., "The NATO STO AVT-201 Task Group on Extended Assessment of Stability and Control Prediction Methods for NATO Air Vehicles: Summary, conclusions and lessons learned," *32nd AIAA Applied Aerodynamics Conference*, Atlanta, Georgia, 2014, AIAA-2014-2394.